

RESEARCH ARTICLE

10.1002/2016JA023475

Special Section:

Major Results From the MAVEN Mission to Mars

Key Points:

- This study presents an analysis of the observations of atmospheric wave perturbations in multiple species in the Martian thermosphere
- The observed properties of the waves in different species show that gravity waves are the most likely atmospheric waves seen
- From an estimation of the wave parameters, we show that the net heating or cooling produced by these waves is significant

Correspondence to:

S. L. England,
england@ssl.berkeley.edu

Citation:

England, S. L., G. Liu, E. Yiğit, P. R. Mahaffy, M. Elrod, M. Benna, H. Nakagawa, N. Terada, and B. Jakosky (2017), MAVEN NGIMS observations of atmospheric gravity waves in the Martian thermosphere, *J. Geophys. Res. Space Physics*, 122, doi:10.1002/2016JA023475.

Received 15 SEP 2016

Accepted 18 NOV 2016

Accepted article online 19 NOV 2016

MAVEN NGIMS observations of atmospheric gravity waves in the Martian thermosphere

S. L. England¹ , G. Liu¹ , E. Yiğit² , P. R. Mahaffy³ , M. Elrod³ , M. Benna³ , H. Nakagawa⁴ , N. Terada⁴ , and B. Jakosky⁵ 

¹Space Sciences Laboratory, University of California, Berkeley, California, USA, ²Department of Physics and Astronomy, George Mason University, Fairfax, Virginia, USA, ³Goddard Space Flight Center, National Aeronautics and Space Administration, Greenbelt, Maryland, USA, ⁴Department of Geophysics, Tohoku University, Sendai, Japan, ⁵Laboratory for Atmosphere and Space Physics, University of Colorado Boulder, Boulder, Colorado, USA

Abstract Gravity waves have a significant impact on both the dynamics and energy budget of the Martian thermosphere. Strong density variations of spatial scales indicative of gravity waves have previously been identified in this region by using in situ observations. Here we use observations from the Neutral Gas and Ion Mass Spectrometer (NGIMS) mass spectrometer on Mars Atmosphere and Volatile Evolution Mission to identify such waves in the observations of different atmospheric species. The wave signatures seen in CO₂ and Ar are almost identical, whereas the wave signature seen in N₂, which is lighter and has a larger scale height, is generally smaller in amplitude and slightly out of phase with those seen in CO₂ and Ar. Examination of the observed wave properties in these three species suggests that relatively long vertical wavelength atmospheric gravity waves are the likely source of the waves seen by NGIMS in the upper thermosphere. A two-fluid linear model of the wave perturbations in CO₂ and N₂ has been used to find the best fit intrinsic wave parameters that match the observed features in these two species. We report the first observationally based estimate of the heating and cooling rates of the Martian thermosphere created by the waves observed in this region. The observed wave density amplitudes are anticorrelated with the background atmospheric temperature. The estimated heating rates show a weak positive correlation with the wave amplitude, whereas the cooling rates show a clearer negative correlation with the wave amplitude. Our estimates support previous model-based findings that atmospheric gravity waves are a significant source of both heating and cooling.

1. Introduction

Understanding the state of the upper atmosphere of Mars, and the processes that control it, is one of the main goals of NASA's Mars Atmosphere and Volatile Evolution Mission (MAVEN). Understanding this region has important consequences for topics as diverse as planning the aerobraking portions of mission to Mars, to constraining the source population of particles for atmospheric escape processes. Early in situ observations of this region, derived from accelerometer data taken during the aerobraking phase of Mars Global Surveyor, Mars Odyssey, and Mars Reconnaissance Orbiter, have revealed that the density of the atmosphere in this region is both highly variable, and often spatially periodic, which is indicative of internal atmospheric waves [e.g., Keating *et al.*, 1998, 2001; Wilson, 2002; Withers *et al.*, 2003; Fritts *et al.*, 2006; Tolson *et al.*, 2007]. From such observations, different classes of atmospheric waves have been identified in this region, including Rossby waves (planetary scale and periods of several Martian solar days (sols) [e.g., Moudden and Forbes, 2010]), thermal tides (planetary scale and periods of integer fractions of 1 sol [e.g., Keating *et al.*, 1998; Wilson, 2002; Withers *et al.*, 2003; Wang *et al.*, 2006; Tolson *et al.*, 2007; England *et al.*, 2016]), and gravity waves (spatial scales of tens to hundreds of kilometers and periods of minutes to hours [e.g., Fritts *et al.*, 2006; Withers, 2006; Creasey *et al.*, 2006; Tolson *et al.*, 2007; Moudden and Forbes, 2010; Bougher *et al.*, 2015; Yiğit *et al.*, 2015a]). The significance of internal waves for the energy and momentum budget of planetary upper atmospheres is being increasingly appreciated, in particular on Earth and Mars [Yiğit and Medvedev, 2015].

Gravity waves (GWs) in the Martian thermosphere have been observed to have a wide range of spatial scales. The most commonly reported spatial scales (e.g., 20–200 km [Withers, 2006] and 100–300 km [Creasey *et al.*, 2006]) are sufficiently short that the entire wave can be observed within a single orbit. Conversely, the temporal persistence of these small-scale waves is too short for the same wave to be observed on multiple orbits, which often take many hours to revisit the same location on the planet. The largest-scale inertial gravity

waves, reported by *Moudden and Forbes* [2010], are global in scale and persist over many days, allowing their character to be determined by using many orbits of observations. In the lower thermosphere ($\sim 100\text{--}150$ km), GWs have been observed to have large amplitudes (relative perturbation compared to the background density, $\rho'/\bar{\rho} \sim 5\text{--}50\%$ [e.g., *Fritts et al.*, 2006]). The amplitudes of these waves have been shown to vary significantly with location, which may be indicative of filtering by longer-period atmospheric waves [*Fritts et al.*, 2006] and/or the impact of various GW dissipative processes [*Yiğit et al.*, 2008]. The amplitude of these waves has also been reported to vary in response to lower atmosphere dust activity [e.g., *Tolson et al.*, 2007]. In the upper thermosphere ($\sim 150\text{--}200$ km), GWs have been observed to have similar amplitudes [*Yiğit et al.*, 2015a]. The amplitudes of these waves have been seen to vary with local time, being significantly stronger on the nightside than the dayside at the same latitude and season [*Yiğit et al.*, 2015a]. As previous Martian general circulation modeling studies [*Medvedev et al.*, 2011b] demonstrated significant direct GW propagation into the thermosphere, there is appreciable evidence that a significant portion of the GWs observed at thermospheric altitudes primarily originate in the lower atmosphere, although the observed amplitudes of these waves at thermospheric altitudes do not simply reflect the spatial distribution of known sources of such waves in the lower atmosphere [e.g., *Creasey et al.*, 2006]. Observing gravity wave propagation directly from the lower atmosphere to the thermosphere is not currently possible, but their signatures have been observed and modeled in the lower atmosphere [e.g., *Creasey et al.*, 2006; *Pettengill and Ford*, 2000; *Altieri et al.*, 2012] and middle atmosphere [e.g., *Wright*, 2012; *Melo et al.*, 2006]. Combining such observations in a coordinated manner may allow future studies to elucidate the connection between the lower atmosphere sources and the properties of these waves at higher altitudes. By including the effects of the background atmosphere and the associated effects of physics-based dissipation processes on gravity wave propagation from the lower to the upper atmosphere, *Yiğit et al.* [2015a] were able to reproduce some of the observed features of these waves in the upper thermosphere, but it is clear that understanding the behavior and characteristics of these waves is an important part of understanding the processes that control the Martian thermosphere.

Much of what is known about the impacts of atmospheric gravity waves on the Martian thermosphere comes from simulations of these waves. Using the extended nonlinear GW parameterization developed by *Yiğit et al.* [2008] in the Max Planck Institute Martian General Circulation Model (MGCM), *Medvedev et al.* [2011a, 2011b] demonstrated that the momentum associated with upwardly propagating gravity waves could significantly impact the general circulation of the Martian thermosphere. Motivated by these findings, the subsequent general circulation modeling study of *Medvedev and Yiğit* [2012] incorporated the dynamical and thermal effects of GWs from the *Yiğit et al.* [2008] scheme, following the procedure outlined in the work by *Yiğit and Medvedev* [2009], and demonstrated that this could contribute significantly to the polar warming observed by Mars Odyssey [*Keating et al.*, 2003]. The significance of such waves in contributing to the energy budget of the Martian thermosphere has been investigated recently in more detail in the work by *Medvedev et al.* [2013, 2015], who have demonstrated that these waves can generate both significant heating and cooling, at times comparable to the solar insolation in this region. *Medvedev et al.* [2013] found a strong cooling in the polar region, and a weaker heating at low latitudes, although the overall spatial pattern is complex. Using a stand-alone one-dimensional full wave model and a prescribed background atmosphere, *Parish et al.* [2009] and *Walterscheid et al.* [2013] have also computed heating and cooling induced by atmospheric gravity waves in the Martian thermosphere. *Parish et al.* [2009] noted significant heating and cooling at different altitudes, depending on the characteristics of the chosen input wave. *Walterscheid et al.* [2013] demonstrated that the heating from atmospheric gravity waves could contribute to atmospheric escape via the Jeans escape process [*Jeans*, 1925]. All of the above studies have highlighted the importance of the heating and cooling induced by gravity wave dissipation at thermospheric altitudes, but it is worth noting that all of these estimates are derived from models, and so far no observationally derived estimates of these heating and cooling rates have been made. Thus, it is the next necessary logical step to provide an observational estimate of GW thermal effects.

Atmospheric gravity wave properties and heating rates have been determined from in situ thermospheric observations with mass spectrometers at other planets. The first such observations were made at Earth with the AE-C satellite. Small-scale waves were identified in simultaneous observations of different atmospheric species (N_2 , He, Ar, and O). Differences in the phase and amplitude of the wave signatures in each species were noted [*Reber et al.*, 1975; *Potter et al.*, 1976; *Hedin and Mayr*, 1987]. These variations were interpreted by using linear models of acoustic-gravity waves that reproduced amplitude and phase variations similar

to those observed [Dudis and Reber, 1976; Del Genio et al., 1978, 1979]. Similar observations of small-scale waves in the thermosphere of Venus were made with the Pioneer Venus Orbiter Neutral Mass Spectrometer, which observed waves in He, N, O, N₂, and CO₂. Kasprzak et al. [1988, 1993] showed that the waves observed in He were typically out of phase with the heavier species. Finally, observations made in the thermosphere of Titan with the Cassini Ion Neutral mass Spectrometer (INMS) have revealed similar small-scale waves in N₂, CH₄, and minor species [e.g., Müller-Wodarg et al., 2006; Cui et al., 2013, 2014]. Cui et al. [2014] used a linear two-fluid model developed by Cui et al. [2013] to find the best fit gravity wave properties that matched the observed wave characteristics seen by Cassini INMS. Using these estimates, Snowden and Yelle [2014] derived the heating and cooling rates associated with the waves observed. Recently, Yiğit et al. [2015a] reported observations of small-scale waves in the upper thermosphere of Mars with the MAVEN Neutral Gas and Ion Mass Spectrometer (NGIMS). This study used the extended nonlinear gravity wave parameterization of Yiğit et al. [2008] to simulate the propagation of a broad spectrum of waves from the lower atmosphere to the upper thermosphere and compared these with observations of small-scale waves in the CO₂.

Here we perform a comprehensive study of the small-scale wave fluctuations observed by MAVEN NGIMS. By comparing the signatures of these waves in different atmospheric species (primarily CO₂, Ar, and N₂), we are able to provide constraints on both the class of wave that is observed and estimate the wave's intrinsic parameters by using a linear two-fluid model to find the best fit to the observed parameters. From our estimates of the wave properties, we determine the approximate heating or cooling rate associated with these waves. Section 2 describes the NGIMS data. Section 3 outlines our method for identifying wave perturbations. Section 4 describes the wave properties seen in different atmospheric species during May 2015. Section 5 reports the monthly mean observed properties from February 2015 to March 2016. Section 6 describes our estimate of the wave intrinsic properties and atmospheric heating and cooling rates.

2. The NGIMS Atmospheric Density Data

The NGIMS instrument on MAVEN is a quadrupole mass spectrometer, capable of measuring the density of the both neutral gas and ions in Mars' upper atmosphere between 2 and 150 amu [Mahaffy et al., 2014]. The MAVEN spacecraft is in a highly eccentric orbit, with periapsis around 150 km and apoapsis around 6220 km above the areoid [Jakosky et al., 2015]. The NGIMS instrument is used to measure atmospheric densities when the spacecraft is at altitudes below 500 km above the areoid. The analysis presented here requires the determination of perturbations to the measured atmospheric density, which requires sufficient signal to determine these perturbations well above the noise level of the instrument. For this reason, all analysis presented here will be restricted to altitudes below 250 km above the areoid (see Figure 1).

NGIMS is described in detail in the work by Mahaffy et al. [2014]. Briefly, in routine science operations, the instrument samples selected mass densities in the range from 2 to 150 amu by using a combination of its closed and open source channels. While the closed source channel is used to measure nonreactive species only, the open source channel is able to measure both reactive and nonreactive species (e.g., CO, NO, O, and ions). On alternate orbits, the open source channel is used to measure either reactive ion species or reactive neutral species—thus, observations of nonreactive neutral species (primarily CO₂, Ar, N₂, and He) are available on every orbit in closed-source mode. When in neutral mode, observations of mass 40 (Ar) in the closed source channel are used to cross-calibrate with the mass 40 (Ar) observations made with the open source channel [Mahaffy et al., 2014]. In neutral mode, the NGIMS instrument measures the density of particles having a particular mass. Processing of these raw counts to observed densities of various species requires accounting for several effects. First, it is possible for more than one atmospheric species to appear in the same mass channel. For example, both CO and N₂ have a mass of 28 amu for their most abundant isotopes. Therefore, the interpretation of counts from certain mass channels does not always lead directly to the density of a particular species. Second, it is possible for molecular species entering the NGIMS instrument to split into their atomic and molecular components (referred to as fractionation). For example, ²⁸N₂ entering the instrument can produce a signal in both the mass 28 and mass 14 channels. Knowledge of the fractionation patterns, along with signals from multiple mass channels, is used to determine the actual number density of each species from the raw NGIMS observations. The NGIMS instrument has a large dynamic range, but to be able to provide continuous measurements of all species of interest of the entire altitude range desired, the instrument measures species with and without attenuation. The calibration between the attenuated and

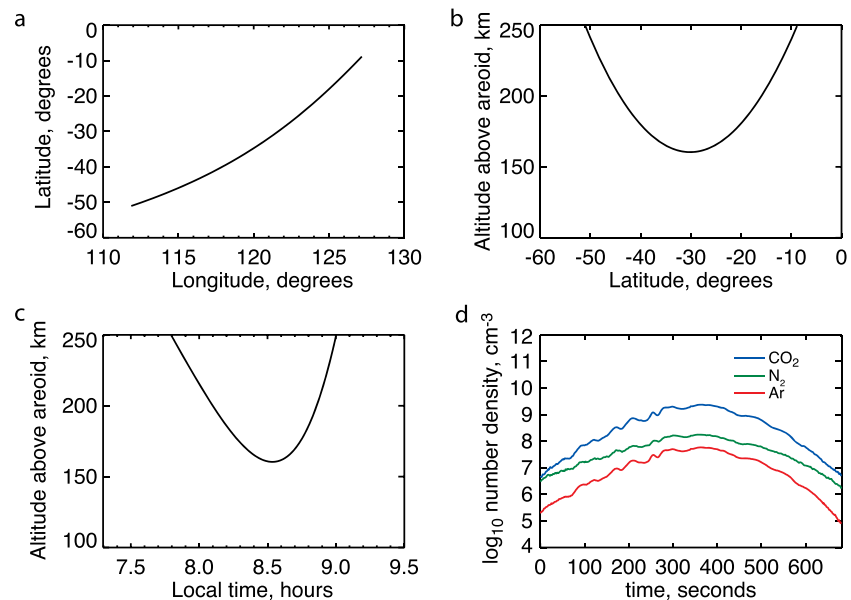


Figure 1. NGIMS sampling for an example periapsis pass, starting when the MAVEN spacecraft crossed 250 km above the areoid on the inbound segment of its orbit on 1 May 2015, 09:33:12 UT. (a) The segment of the orbit below 250 km above the areoid as a function of latitude and longitude (east positive). (b) The segment of the orbit as function of altitude above the areoid and latitude. (c) The segment of the orbit as function of altitude above the areoid and local time. (d) The \log_{10} number density of CO_2 , Ar, and N_2 observed by NGIMS as a function of time during this periapsis pass. For this particular pass, periapsis occurred around 160 km, at 30° south, 122° east and 8.5 h local time, and the spacecraft spent 682 s below 250 km above the areoid.

nonattenuated observations is done by using measurements from altitude regions in which a clear signal is observed in both. All of the calibrations noted above have been applied to the Level 2, version 06, revision 01 data that will be used as part of this study.

Given that reactive neutral species and ions are measured only on alternate orbits, this study will focus primarily on the nonreactive neutral species $^{44}\text{CO}_2$, ^{40}Ar , and $^{28}\text{N}_2$. The number densities observed for each of these species throughout an example periapsis pass are shown in Figure 1d. The most significant trend seen is the exponential increase in number density of all three species with decreasing altitude, maximizing close to periapsis. This is as expected for species that are not formed by photodissociation or photoionization. However, superimposed on this general trend are clear wave-like perturbations that can be seen in all three species (significant wave activity is visible during the inbound portion of this orbit from around 100 to 300 s during this pass, corresponding to ~ 165 –205 km altitude, with substantially less activity present on outbound portion of this orbit). The amplitude of these oscillations increases with the background atmosphere such that the density perturbations remain a significant fraction of the total density at all altitudes. Given that this periapsis pass lasts for 660 s, during which the spacecraft travels approximately 2500 km along its track and subtends an altitude range of approximately 85 km, it is clear that the NGIMS instrument is sampling wave activity that extends over a large region.

Before attempting to quantify the properties of the wave (such as its wavelength), or attempting to attribute this to any particular class of atmospheric wave, it is worthwhile to consider the geometry of the in situ NGIMS observations. If the spacecraft moved purely vertically, the wavelength seen along the spacecraft trajectory (referred to as apparent wavelength hereafter) would be relatable to the vertical wavelength of the waves present (given the relative speeds of the spacecraft and phase velocities of the waves, it is a relatively good approximation to neglect the motion of the waves within the time of the observation, so Doppler shifting within the spacecraft frame can be ignored). However, this geometry is not the case for any realistic spacecraft orbit. Close to periapsis, the spacecraft is moving essentially horizontally, and thus is sampling purely horizontal structures. Yet even in this region relating the apparent wavelength to the horizontal wavelengths of the actual waves present is complicated by lack of knowledge of the spacecraft ram vector relative to the wave's phase velocity and the presence of more than one wave in any sample volume. At altitudes above

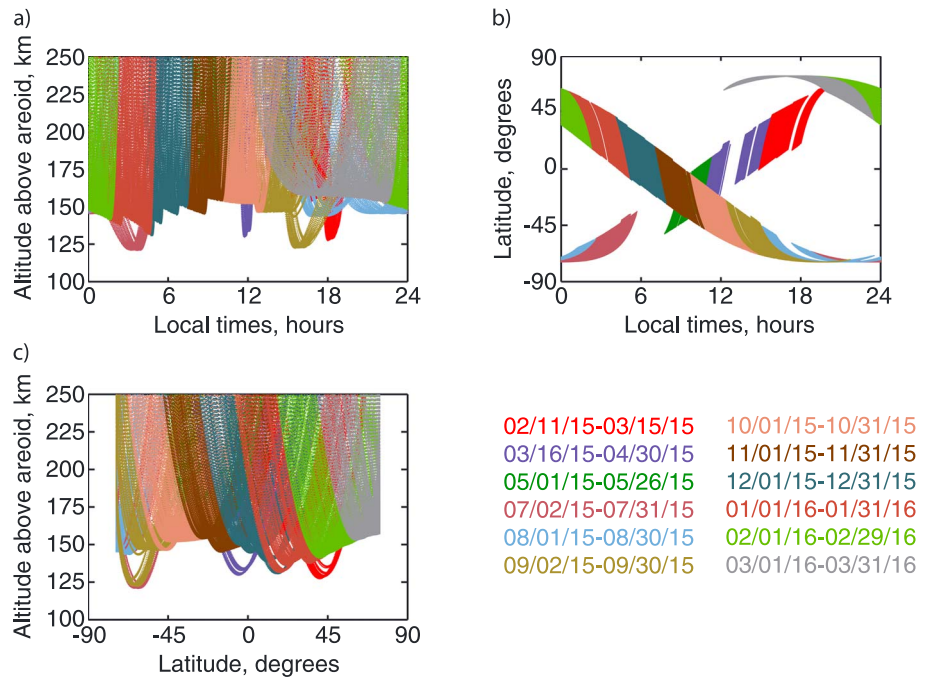


Figure 2. Coverage of the NGIMS data included in this study. In each of the panels, a small dot has been plotted at the location of every fifth sample of CO₂ made by NGIMS. The color-coding corresponds to data taken within the date ranges listed. (a) The coverage as a function of altitude above the areoid and local time. (b) The coverage as a function of areographic latitude and local time. (c) The coverage as a function of altitude above the areoid and areographic latitude.

periapsis, the sampling geometry is even more complex as both horizontal and vertical structures are convolved. For this reason, we cannot rely solely upon the observed apparent wavelength to infer the wave properties in this study.

Atmospheric wave parameters will be estimated from the differences in their signatures in different species (see section 4 for more details). This approach makes use of multiple orbits of data to provide the mean observed properties of waves each in species. Therefore, it is important that the NGIMS instrument remains in the same operating mode over all observations that will be considered in such an analysis. While regular science operations for NGIMS began in 11 November 2014 the NGIMS settings were changed to a new operating mode on 11 February 2015. Given that the December data were taken by using different instrument operating setting than all subsequent data, these are not included in the present study.

It is worth noting that *Yigit et al.* [2015a] presented an initial analysis of atmospheric waves by using NGIMS data from December 2014. The December time period was selected for that study as it offered a data set in which local time and latitudinal variations could be decoupled from one another. However, the sampling of NGIMS as a function of latitude and local time in December was atypical, and in general, local time, latitudinal, and seasonal variations in the NGIMS observations cannot be easily separated. Thus, in the present study it will not be possible to fully separate local time from latitudinal and seasonal effects.

Figure 2 shows the coverage of all of the NGIMS data that is included in the present study, as functions of altitude, local time, and latitude. In total, 1658 orbits of data are included, which represents over 300,000 samples of the neutral atmosphere. Spacecraft motion is ~ 4.2 km/s and samples every ~ 2.6 s, so smallest sample scale is ~ 11 km along orbit track.

3. Identification of Atmospheric Waves in the NGIMS Data

The identification of atmospheric waves in the NGIMS density observations is done in three steps: the identification of the background density profile, characterization of the oscillations in the density profile, and the perturbations in temperature associated with atmospheric waves.

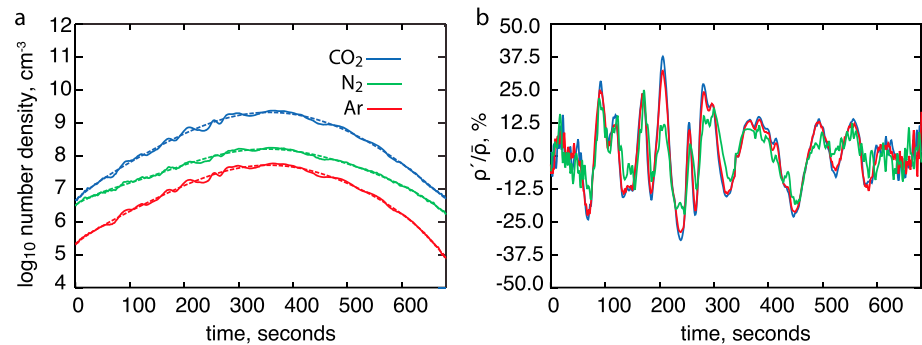


Figure 3. (a) The log₁₀ number density of CO₂, Ar, and N₂ observed by NGIMS as a function of time, starting when the spacecraft reaches 250 km above the areoid on the inbound portion of its orbit. The solid lines show the NGIMS observed density values, and the dashed lines show the corresponding values of $\bar{\rho}$, defined in the text. All data are for the same orbit shown in Figure 1. (b) The values of $\rho'/\bar{\rho}$ as defined in the text, for each of the three species, color-coded to match Figure 3a.

3.1. Identification of the Background Density Profile

In order to determine the observed properties of atmospheric waves in the NGIMS data, the background atmospheric density and the wave-like perturbations on this background must be separated. In order to do this, it is necessary to estimate this background density profile from the NGIMS data (essentially, what the NGIMS density profiles would be in the absence of any wave-like perturbations). For this, we follow the method described in the work by *Yigit et al.* [2015a]. Briefly, a seventh-order polynomial is found by a least squares fit to the log of the density observations made throughout the periapsis pass. This technique is found to provide a good estimate of the background density, allowing for all of the principle variations in the NGIMS observations other than the atmospheric waves to be characterized. Specifically, it provides a good fit to both the exponential increase in density toward periapsis, the variation in the scale heights (and therefore temperature) over the altitude region of interest (from periapsis to 250 km), and the asymmetry between the inbound and outbound portions of the periapsis pass resulting from differences in the latitude, longitude, and local time. Figure 3a shows the seventh-order polynomials fits to each of the three neutral density profiles shown in Figure 1d. Removing this background from the observations provides an estimate of the density perturbation (ρ' hereafter). Normalizing this against the background density ($\bar{\rho}$ hereafter) produces an estimate of the fractional density perturbation ($\rho'/\bar{\rho}$), shown in Figure 3b. Examining $\rho'/\bar{\rho}$, it can be seen that this is oscillatory about a mean value of zero, which demonstrates that the perturbations are indeed wave-like and that the seventh-order polynomial fit is characterizing $\bar{\rho}$ effectively for all three species. The use of a polynomial fit to characterize $\bar{\rho}$ from this kind of in situ density offers an advantage over the more commonly used running mean of the observed density values, used to identify waves in accelerometer data at Mars [e.g., *Fritts et al.*, 2006; *Tolson et al.*, 2008] and wave structures in mass spectrometer data at Venus [e.g., *Kasprzak et al.*, 1988], in that it is not as susceptible to waves with periods longer than the averaging interval which is used (39 s in the case of *Fritts et al.* [2006]). The polynomial fit used here is similar to that which has been used successfully with mass spectrometer data from Titan [*Cui et al.*, 2013, 2014].

Examining Figure 3b, it is clear that wave-like perturbations are present throughout almost the whole of this periapsis pass (which is typical of the NGIMS data set). However, at high altitudes (the first and last ~100 s of this pass, during which the spacecraft is above 205 km altitude), the signal is less clear, possibly because the waves themselves are less evident, or less strong relative to the instrument noise level. For this reason, we will limit all analysis presented here to exclude the first and last 100 s of each periapsis pass (and therefore to altitudes below ~205 km).

Using the profile of $\bar{\rho}$, it is straightforward to estimate the scale height of the atmosphere by assuming hydrostatic equilibrium. If the temperature is common to all neutral species at any one altitude, the scale height should vary between each species (i.e., N₂ will have a larger scale height than Ar or CO₂, given its relatively lower mass), and therefore, the scale heights for each species are found independently. From an examination of numerous periapsis profiles (not shown here), we have found that it is not possible to determine the scale height accurately in the region close to periapsis. This may be expected because as the spacecraft trajectory is

almost completely horizontal, it is not possible to separate horizontal from vertical variations in density (either background or associated with waves) from vertical (hydrostatic or associated with waves) variations. By inspection, it is determined that the typical maximum density perturbation near periapsis is ~35% of the background density, which is approximately the same density variation observed when the spacecraft moves vertically through one third of a scale height (approximately 5 km for CO₂ or Ar). For this reason, scale heights are not determined for altitudes within 5 km of periapsis on any given pass. For the orbit shown in Figures 1 and 3, this limits this analysis to altitudes above ~165 km. The scale heights, along with the background densities, are required for the analysis of atmospheric waves presented in section 6, and as such, our analysis will be confined to regions in which all of these properties can be reliably determined.

3.2. Characterization of the Oscillations in the Density Profile

To determine the properties of the waves observed by NGIMS, it is useful to identify the phase, amplitude, and apparent wavelength of each of the waves observed, during each of the 1658 orbits considered here. To do this, a two-step fitting process is used to identify the apparent wavelengths, amplitudes, and phases of each of the waves seen. This method differs from that used to analyze similar mass-spectrometer data at Titan by Müller-Wodarg *et al.* [2006], in that it allows for the apparent wavelengths to change as function of altitude, which occurs as a result of either changes in the background atmosphere, or wave dissipation, and allows for the presence of more than one wave at different points throughout the orbit, which is necessary to account for the large degree of asymmetry in the wave-field seen between inbound and outbound portions of the orbit seen by NGIMS (see Figure 3b).

The first step is to identify the apparent wavelengths of the oscillations seen in each periapsis pass. This step is done by using a Lomb-Scargle spectral analysis [Lomb, 1976; Scargle, 1982], which is applied to a rolling 100 s window of the Ar density observations. A rolling window is used as this allows the waves identified to change from one region to another. The same could be achieved with a wavelet analysis, but the Lomb-Scargle spectral analysis is more robust to missing or unequally sampled data, which occurs sporadically throughout the data set. One hundred seconds is chosen based on the longest apparent wavelengths typically seen in the NGIMS observations. Note that while the data within 5 km of periapsis and above ~205 km are excluded in subsequent analyses, the Lomb-Scargle spectral analysis is performed on all of the data in order to avoid any edge effects. Ar is selected as there are high-quality observations of Ar over a wide range of altitudes on all orbits, but essentially identical results are achieved if CO₂ is used. The confidence interval associated with each wave identified in the Lomb-Scargle analysis is computed, and only those exceeding 80% are kept. Finally, the apparent wavelengths of the three largest-amplitude waves are recorded. The NGIMS instrument samples neutral species every ~2.6 s, which are interpolated to a 2 s cadence in generating the Level 2 data product, so any apparent wavelengths found with periods below 6 s are dismissed.

In the second step, a least squares fit to the $\rho' / \bar{\rho}$ time series is performed, using the apparent wavelengths as a function of time throughout the periapsis pass found in step 1. This least squares fit is used to find the amplitude and phase of each of the waves identified, in each of the three species. Figure 4a shows the reconstruction of these waves, against the original $\rho' / \bar{\rho}$ values from Ar for the same orbit shown in Figure 3. As can be seen, the waves identified in this method are able to capture all of the key features of $\rho' / \bar{\rho}$.

3.3. Determination of the Temperature Perturbations Associated With Atmospheric Waves

Using the time series of density measurements, it is also possible to determine the atmospheric pressure and temperature perturbations associated with the waves seen. Following the method described in the work by Snowden *et al.* [2013], this is done by first determining the atmospheric pressure from the density measurements, assuming hydrostatic balance, and then converting these to temperatures using the ideal gas law. The conversion from density to pressure using hydrostatic balance requires integration with altitude, starting from the measurements at the highest altitude on the inbound portion of the orbit (250 km in this case), and running through periapsis to the end of the outbound portion of the data. This integration requires an estimate of the pressure at the initial point in the integration (p_0 , corresponding to the pressure at 250 km on the inbound portion of the orbit). Following Snowden *et al.* [2013], p_0 is determined from the scale-height-derived temperature T_0 , the measured density, and ideal gas law.

The observed density values are used to find the observed temperatures, and the background density profile described in section 3.1 is used to derive a background temperature profile. This then allows the temperature

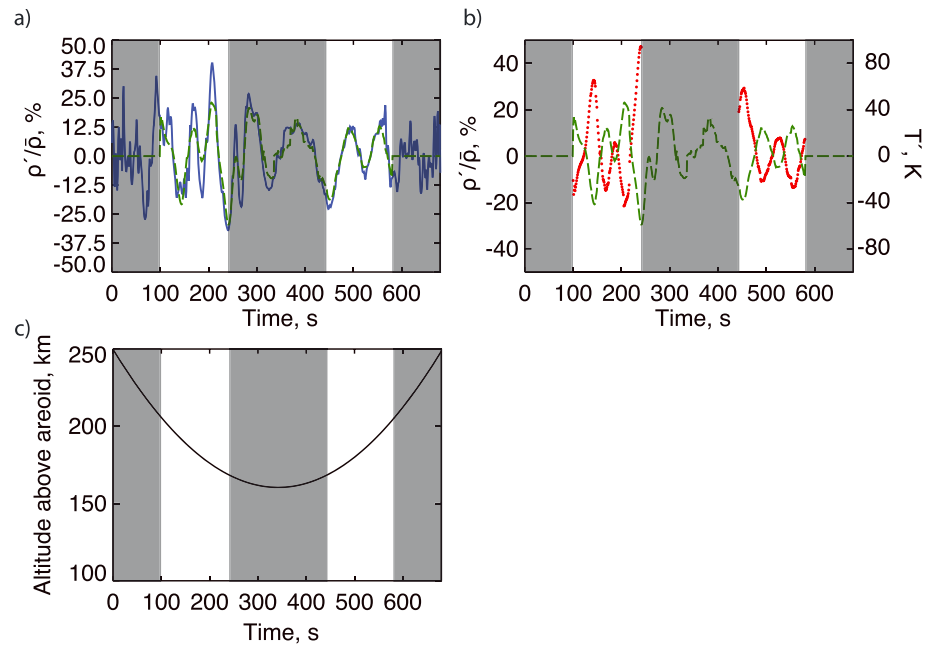


Figure 4. (a) The time series of $\rho'/\bar{\rho}$ for Ar (blue) and the reconstruction of the least squares fit to this (green dashed), for the same orbit as shown in Figure 1. Regions within 5 km of periapsis and within the first and last 100 s of the pass (approximately above 205 km) are shaded and are excluded from subsequent analysis. (b) The same as Figure 4a, but for the time series of the reconstruction of the least squares fit to $\rho'/\bar{\rho}$ for Ar (green) and the temperature perturbations derived from the densities (red). (c) The altitude of MAVEN as a function of time during this orbit.

perturbation (T') to be found in the same manner as the density perturbation (ρ'). This same procedure has been performed on the CO_2 and Ar densities (not shown), and the resultant background temperature profiles are found to be in good agreement. For all calculations involving this background temperature, those derived from Ar will be used, as the observed Ar densities are not subject to any perturbation by photochemistry or other effects that might modify the computed background temperature.

As described in Snowden *et al.* [2013], the derived values of T and T' rely on the assumption that all of the density variations seen along the orbit are associated with changes in altitude. In regions of strong horizontal gradients, or when the spacecraft is flying principally horizontally, this assumption is not valid and the uncertainty in the derived values of T and T' becomes large and difficult to quantify. As the spacecraft trajectory is quasi-horizontal at altitudes close to periapsis, these effects are most significant in this region, and thus, all data from within 5 km of periapsis will be removed from our analysis. The resulting profile of derived T' and the reconstruction of the wave-fits to this is shown in Figure 4b.

The analysis described above relies upon the assumptions that the changes in density with altitude can be converted to atmospheric temperature by using the assumptions of hydrostatic balance and the ideal gas law. Further, interpreting the temperatures derived from the Ar observations as a characteristic atmospheric temperature relies upon the assumption that different neutral species have a similar temperature at these altitudes. Given that atmospheric species are not well mixed in the thermosphere, and that nonlocal thermodynamic equilibrium effects associated with radiative heating and cooling of CO_2 are important at these altitudes [e.g., López-Valverde and López-Puertas, 1994], it is worth exploring the validity of these assumptions and possible consequences on the analysis presented here.

Using hydrostatic balance and vertical changes in the observed density of a particular atmospheric species to derive temperature assumes that there are no sources or sinks of that atmospheric species. At thermospheric altitudes, neutral species can be destroyed by chemical reaction, photodissociation, and photoionization. For the case of Ar, used here, chemical reactions and photodissociation can be ignored, but photoionization can potentially impact the computation of a temperature from the Ar density observations. The NGIMS instrument is able to measure Ar^+ (or specifically ions with a mass to charge ratio of 40 amu). Taking the example

of May 2015, the monthly mean ratio of $[\text{Ar}^+]/[\text{Ar}]$ at all altitudes below 250 km is below 1%, which suggests that for Ar, this effect can also be ignored at the altitudes considered here.

Recently, *Medvedev et al.* [2016] have derived thermospheric temperatures from MAVEN observations of CO_2 density observations and compared these to temperatures simulated by using the first-principles Max Planck Institute MGCM model, which includes nonlocal thermodynamic equilibrium CO_2 heating and cooling effects. The good agreement between the model and observations suggests that a similar approach using CO_2 to derive a single temperature for the Martian thermosphere may also be reasonable. Using the NGIMS data, it is possible to compare the temperatures derived from observation of Ar, CO_2 , and N_2 using the method described above, which can provide a measure of confidence in the derived temperatures, and estimate the impact of both photodissociation and nonlocal thermodynamic equilibrium effects on the derived temperatures, as these effects vary significantly between these three species. Following the method outlined above, we have determined the atmospheric temperature for each of these three species for all 117 orbits during May 2015. The mean and standard deviations of the temperatures derived in the altitude region described above for Ar are 241 ± 37 K, for CO_2 243 ± 29 K, and for N_2 239 ± 25 K. While the standard deviations differ, the mean values derived for all three atmospheric species are within $\pm 1\%$, which suggests that a single temperature approximation is appropriate within this region and that nonlocal thermodynamic equilibrium effects that impact the radiative heating and cooling of CO_2 are not significantly impacting the temperatures derived by using the NGIMS density observations. Further, it is expected that the temperature perturbations derived from the Ar and CO_2 profiles should be similar (see section 3.1). Examining these values using all data from May 2015, we find that the mean temperature perturbation derived from the Ar observations is 16.8 K and the mean temperature perturbation derived from the CO_2 observations is 18.2 K. Again, the high degree of agreement between these two (a difference of 8%) suggests that using the Ar density observations to derive bulk temperature perturbations associated with atmospheric waves is a good approximation.

4. Observed Properties of the Wave Signatures

By examining either individual orbits or the mean properties seen over 1 month of observations, the characteristics of the wave perturbations seen in each of the species measured by NGIMS can be identified. In the sections to follow, we will next highlight some of the typical wave properties, such as amplitude, apparent period, and phase, with respect to the different observed species. Dependence of amplitudes on wave period and altitude will be investigated.

4.1. General Characteristics

Visual inspection of the time series of $\rho'/\bar{\rho}$ (e.g., Figure 3b) reveals that obvious wave features in almost all orbits of the NGIMS data. The most easily identifiable wave features have apparent wavelengths of several tens to hundreds of kilometers and relative amplitudes of $\sim 10\%$. To examine the more typical properties of the waves found by using the method described in section 3, we consider 1 month of data. Here the month of May 2015 is selected, for which 116 orbits of NGIMS data are available, and during which time the periapsis of MAVEN sweeps through approximately 2 h of local time from ~ 11 to ~ 9 h LT (see Figure 2). As the measurements from NGIMS at these altitudes have been seen to vary significantly with longitude as a result of planetary-scale waves [*England et al.*, 2016], it is important to average data from all longitudes together to find the mean properties at any given latitude and local time. Figure 5a shows a reconstruction of $\rho'/\bar{\rho}$ as a function of altitude for each orbit during May 2015, where the values of $\rho'/\bar{\rho}$ are determined from the CO_2 observations. Individual large-amplitude waves are visible at all heights from the periapsis up to at least 250 km. The envelope of the relative density perturbations is typically $\leq 40\%$, although occasional waves with amplitudes in the 50–70% range can be seen in this altitude range.

Figures 5b and 5c show the frequency of occurrence of waves at different relative density amplitudes and apparent wavelengths. Figure 5b shows that while waves of amplitude $\geq 10\%$ are not rare, the majority of waves identified by our method are smaller than this. The median relative density amplitude of all waves found during this 1 month of data is 3%. Figure 5c shows the distribution of apparent periods identified. No strong trend is seen here, although it is worth noting that this is dependent upon the selection of the bin size for apparent wavelengths. The median apparent wavelength observed is 120 km along the orbit

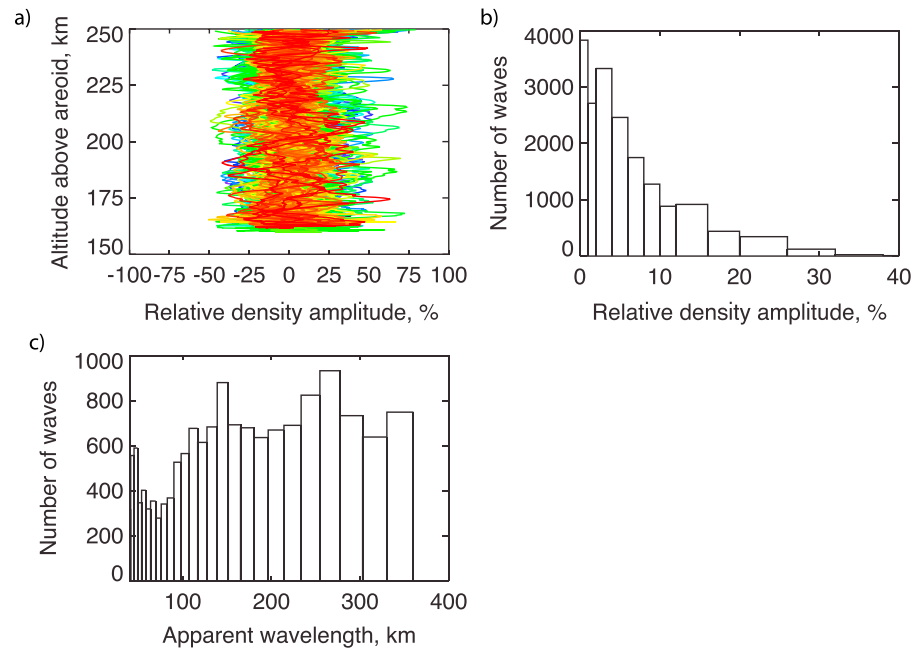


Figure 5. Properties of the waves observed during May 2015. (a) A reconstruction of all waves identified in the CO₂ observations, where each orbit is shown in a different color. Note that only data from 5 km above periapsis to around 205 km are used in the subsequent analysis. (b) The occurrence of waves detected with different relative density amplitudes. (c) The same as Figure 5b but for different apparent period of the waves. Note the nonuniform bin size used in both Figures 5b and 5c.

track. The amplitude and apparent wavelengths seen are in basic agreement with in situ accelerometer observations *Fritts et al.* [2006], although the accelerometer observations correspond to lower altitudes (~100–150 km) than those examined here.

4.2. Differences Resulting From Species-Dependent Scale Heights

Figure 3b suggests that the same large-amplitude waves affect all three species in a similar manner. However, the values of $\rho' / \bar{\rho}$ are not the same in all species. The response of CO₂ and Ar to the waves present is almost exactly the same, which may be expected as these two species have almost the same mass (40 and 44, respectively) and same scale height. The values of $\rho' / \bar{\rho}$ for N₂ are often smaller than for the two heavier species, and at times the waves seen in N₂ appear to be slightly out of phase with those in CO₂ and Ar (see, for example, around 330 s, where the minima in N₂ appears to lag that in CO₂ and Ar). Such variations in the amplitude and phase of wave seen in different species in mass spectrometer data have been reported in previous observations, such as those from the upper atmosphere of Earth [e.g., *Reber et al.*, 1975] and Venus [e.g., *Kasprzak et al.*, 1988], both of which noted that the waves seen in He were out of phase with those seen in heavier species and that the heavier species typically saw larger-amplitude perturbations than those in He.

This behavior may be expected from a simple consideration of the ways in which internal waves can modify the in situ density for a particular species. As noted by *Dudis and Reber* [1976], the density perturbations seen in situ result from two effects: the first is divergence of the flow and the second is vertical advection of fluid parcels. This can be illustrated by writing the continuity equation for linear, plane wave perturbations in the absence of rapid diffusion as

$$\frac{\tilde{\rho}}{\bar{\rho}} = \frac{i}{\omega} \left(\frac{\tilde{w}}{H_i} - \nabla \cdot \tilde{V} \right), \quad (1)$$

where ω is the wave frequency, \tilde{w} is the vertical velocity perturbation, H_i is the species-dependent scale height, and \tilde{V} is the velocity perturbation. As discussed in *Cui et al.* [2014], in the long-wavelength limit, the first term will dominate and the relative density perturbation in each species will scale with $1/H_i$, whereas in the short-wavelength limit the second term will be dominant, which is common to all species. The effect of

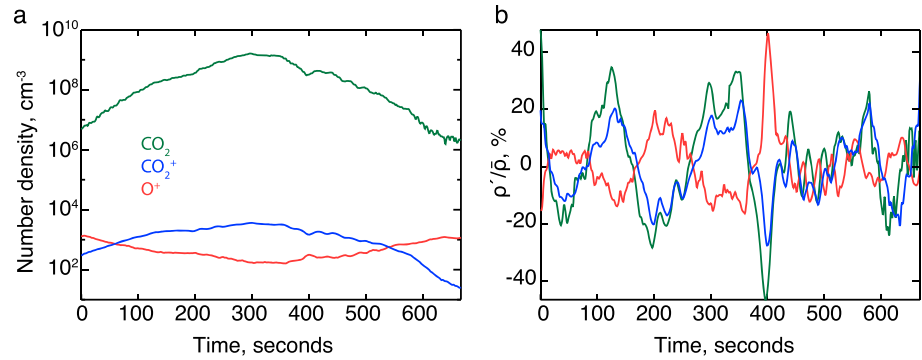


Figure 6. Number density of CO₂, CO₂⁺, and O⁺ during a periapsis pass on 2 March 2015. (a) The observed number density as a function of time when the spacecraft is below 250 km above the areoid. (b) The relative density perturbation in each species, color-coded to match Figure 6a.

variations associated with species scale height can be illustrated by selecting an orbit in which predominantly long-wavelength waves are observed. Figure 6 shows such an illustrative example for an orbit during 2 March 2015. Here the species selected are CO₂, CO₂⁺, and O⁺. CO₂ and CO₂⁺ have the same mass, and from Figure 6a, it is clear that they have similar scale heights. O⁺ is a much lighter species (mass 16 relative to mass 40), and for the conditions of this particular orbit (which corresponds to late afternoon, from ~0 to 45° north and is away from any strong crustal magnetic fields), the periapsis of the spacecraft is below the peak of the O⁺ layer (the altitude of the O⁺ peak is around 250 km for this orbit). This is seen in Figure 6a as a decrease in O⁺ density as the spacecraft altitude decreases, which would correspond to a negative scale height in this region. This extreme case for the difference in scale height of O⁺ compared to CO₂ and CO₂⁺ should produce a very different response to longer-wavelength internal waves, according to equation (1). This response is shown in Figure 6b. Here the response of the relative density of CO₂ and CO₂⁺ to the waves present is in broad agreement: the two species show comparable amplitude variations and are generally in-phase. The response seen in O⁺ to the waves present is an almost completely out-of-phase response in its relative density, compared to CO₂. This behavior would be expected from equation (1), given the negative scale height of O⁺ in this region. This can be thought of intuitively as the result of vertical advection of a parcel of gas, where an upward (downward) transport would bring gas that contains more (less) CO₂ per unit volume and less (more) O⁺ per unit volume up to the altitude at which it is observed.

4.3. Variation in Amplitude With Apparent Period

Numerous previous studies have used the apparent wavelength of the wave as seen along the spacecraft orbital track as a proxy for the actual wavelength of waves measured in situ. In the absence of any other measure of the actual wavelength, this provides a convenient means of studying how the observed wave properties may vary as a function of wavelength, which can provide insight into their nature and effects of dissipation. However, in situ observations generally provide insufficient information to determine the actual wavelength, or its horizontal or vertical components, as the angle between the spacecraft velocity and the wave phase velocity is not known. Nonetheless, some general relationship exists between the apparent wavelength measured along the orbital track and the actual wavelength. Thus, even if it is not suitable for a detailed, quantitative analysis, it is still instructive to use the wavelength seen along the orbital track to explore how the properties of the observed waves may vary with wavelength.

Figure 7 shows the power spectral density (PSD) of $\rho'/\bar{\rho}$ measured in CO₂, Ar, and N₂, along with the temperature perturbations, as functions of apparent wavelength. The power spectral densities are derived from all data taken in May 2015 that meet the altitude criteria discussed in section 4.1. The basic behavior of the PSD as a function of apparent wavelength is consistent for all three species and the temperatures. For apparent wavelengths beyond ~200 km, the PSD values do not vary with apparent wavelength. For apparent wavelengths from ~60 to 200 km, the PSD follow a power law, proportional to the apparent wavelength squared. The solid lines plotted in Figure 7 show this power law for reference. This kind of power law in the PSD has been reported from the analysis of observations of Earth's atmosphere [e.g., VanZandt, 1982] and the lower

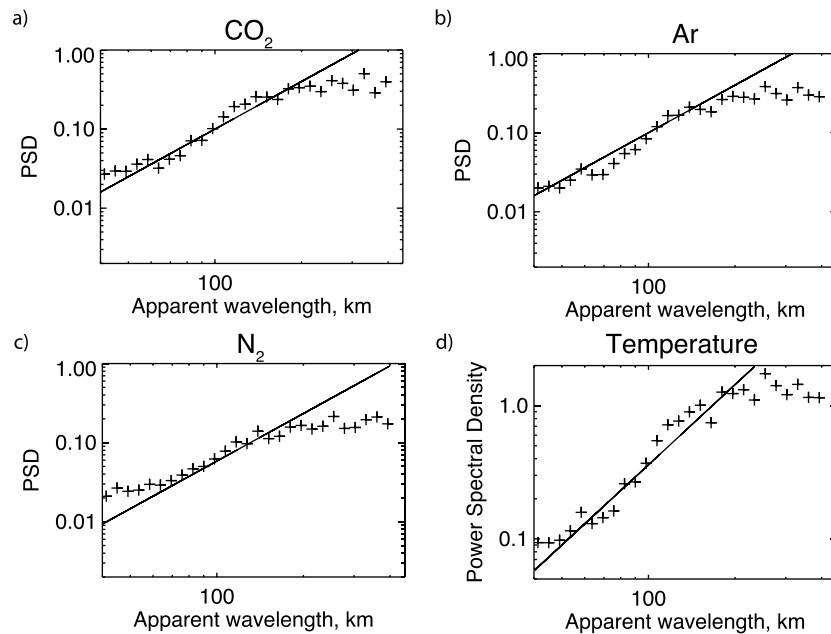


Figure 7. Power spectral densities of $\rho' / \bar{\rho}$ in (a) CO_2 , (b) Ar, (c) N_2 , and (d) in the temperature perturbations, as a function of apparent wavelength as defined the text. Values are computed from all measurements taken in May 2015 below ~ 205 km altitude above the areoid and above 5 km from periapsis, as described in section 4.1. The solid line in each panel shows a slope of power spectral density proportional to apparent wavelength squared, which is shown for reference.

thermosphere of Mars [e.g., *Fritts et al.*, 2006]. The spectral slope of wavelength appears to be common across different atmosphere and locations and is referred to as the universal spectrum. The fact that the observations shown in Figure 7 follow this universal spectrum well is consistent with the apparent wavelength being a reasonable proxy for the true horizontal wavelength. This variation in the PSD with apparent wavelength is consistent with that expected for internal gravity waves in a region above their source, as wave dissipation via viscosity and saturation tend to preferentially damp shorter-wavelength waves as they propagate upward through the atmosphere [see *Fritts and Alexander*, 2003, and references therein].

For apparent wavelengths below ~ 60 km (corresponding to ~ 15 s along the spacecraft track), the PSD depart from the power law slope in all species and the temperatures. This departure is not expected from theory, and instead may be caused by the limitation of the smallest detectable amplitude of a wave by the NGIMS instrument, or the limit of validity of our wave-fitting procedure for these small-scale waves, or the limit of the validity of using the apparent wavelength as a proxy for the true horizontal wavelength at these scales.

4.4. Variation in Amplitude Between Species

As described in section 4.2, we expect $\rho' / \bar{\rho}$ to vary between species. For long-wavelength waves, the $\rho' / \bar{\rho}$ observed in each species should vary in proportion to $1/H_i$. By grouping the waves observed according to their apparent wavelength, it is also possible to investigate how this varies as a function of wavelength. As the scale heights for CO_2 and Ar are similar, we will examine the ratio of $\rho' / \bar{\rho}$ in CO_2 with that observed in N_2 . Figure 8 shows this ratio as a function of apparent wavelength, for all of the observations from May 2015 described in the previous sections. To highlight the underlying trend, the dashed line shows a smooth fit to these data, found using an average of 5 consecutive values.

For apparent wavelengths beyond ~ 100 km, the ratio is approximately constant at a value of ~ 1.4 . This is consistent with the approximation for long-wavelength waves described in section 4.2, as the ratio of H_{N_2} to H_{CO_2} is 1.57 (H_{N_2} is 21.0 km and H_{CO_2} is 13.4 km for this case). For apparent wavelengths below ~ 100 km, the value of this ratio varies with apparent wavelength, decreasing toward a value of ~ 1.2 . This is consistent with a transition toward the small-wavelength approximation to equation (1). For small-wavelength waves, the second term, related to divergence of the flow, dominates. Following the arguments of *Del Genio et al.* [1979], as the flow is similar for all species, this term would be common to all species, leading to a ratio close to 1. Recalling

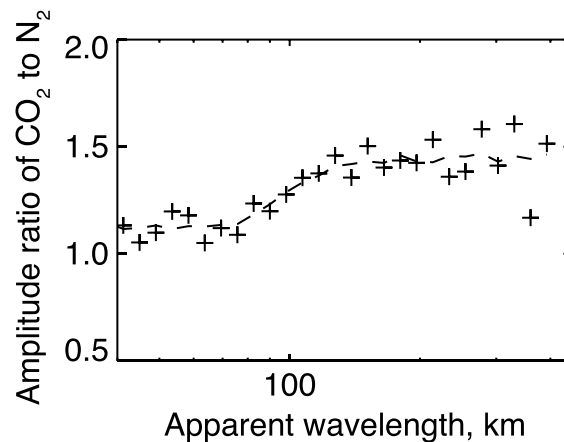


Figure 8. Ratio of $\rho' / \bar{\rho}$ observed in CO₂ to that observed in N₂ as a function of apparent wavelength (km) as defined in the text. Values are computed from all measurements taken in May 2015 below ~205 km altitude above the areoid and above 5 km from periapsis, as described in section 4.1. The dashed line shows a smooth fit to five consecutive ratios, truncated to three consecutive ratios for the largest and smallest apparent wavelengths.

2006; Cui *et al.*, 2013]. While the species observed at each planet vary, all of these prior observations have noted a phase difference between light and heavier species and have noted that waves observed in species of similar masses are approximately in phase with one another. Phase differences have been predicted by theoretical models of the impacts of internal atmospheric waves on the upper atmosphere [e.g., Dudis and Reber, 1976; Del Genio *et al.*, 1978; Cui *et al.*, 2013]. The model of Dudis and Reber [1976] ignored any wave-induced diffusion and assumed all species moved at the same velocity. In this approximation, phase differences arise from the relative importance of vertical advection (a function of H_i) and flow divergence (which is constant) for different species. As noted by the authors, their model is only valid where diffusion is slow compared to the wave period, which corresponds approximately to the lower thermosphere. At higher altitudes, the effects of diffusion should be included, as in the models of Del Genio *et al.* [1978] and Cui *et al.* [2013]. By including wave-induced diffusion, and allowing the velocity to vary by species, the flow divergence term in the continuity equation becomes species-dependent, which Del Genio *et al.* [1979] argued further contributes to phase differences between waves observed in species of difference H_i . Following either the theory of Dudis and Reber [1976], or Del Genio *et al.* [1978], the phase differences between species are expected to vary with wavelength, as the importance of each term in the continuity equation is wavelength-dependent. Del Genio *et al.* [1979] presented the theoretical phase difference versus wave period for gravity waves of different wavelengths, based on the model of Del Genio *et al.* [1978], and showed that the variation in phase versus wave period is complex and varies with wavelength.

Clear variations in the phase of different species can be seen in Figure 6, but it is instructive to investigate how this varies as a function of apparent wavelength, estimated using the data from May 2015 described in the previous sections. Figure 9 shows the phase difference between CO₂ and Ar and CO₂ and N₂ as functions of apparent wavelength during May 2015. Note that only the absolute value of the phase difference is recorded, as the sign of the phase difference depends on the direction of wave propagation relative to the spacecraft velocity, which is unknown. The phase difference between CO₂ and Ar is small (~5–10°) for all apparent wavelengths greater than 100 km, which may be expected for two species of such similar masses and H_i . At shorter apparent wavelengths, the phase difference increases with decreasing apparent wavelength to around 50–60° at the shortest apparent wavelengths. For the phase difference between CO₂ and N₂, the behavior is similar, although the phase difference at apparent wavelengths less than ~100 km is around 30°. While the details depend on the species selected and period of the wave, this overall behavior is consistent with that predicted for internal gravity waves by the model of Del Genio *et al.* [1978], although it is worth noting here that measurement and fitting uncertainty may be significant for the shortest wavelengths shown.

that equation (1) is valid in the case of slow diffusion, and noting that this equation appears to describe the behavior shown in Figure 8, it is reasonable to conclude that at least at the spatial scales sampled by NGIMS, wave dissipation due to diffusion is generally slow compared to the periods of the waves observed.

4.5. Variation in Phase Between Species

Differences in the phase of waves observed in different species have been noted in previous mass spectrometer observations from Earth [e.g., Reber *et al.*, 1975; Potter *et al.*, 1976; Hedin and Mayr, 1987], Venus [e.g., Kasprzak *et al.*, 1988, 1993], and Titan [e.g., Müller-Wodarg *et al.*,

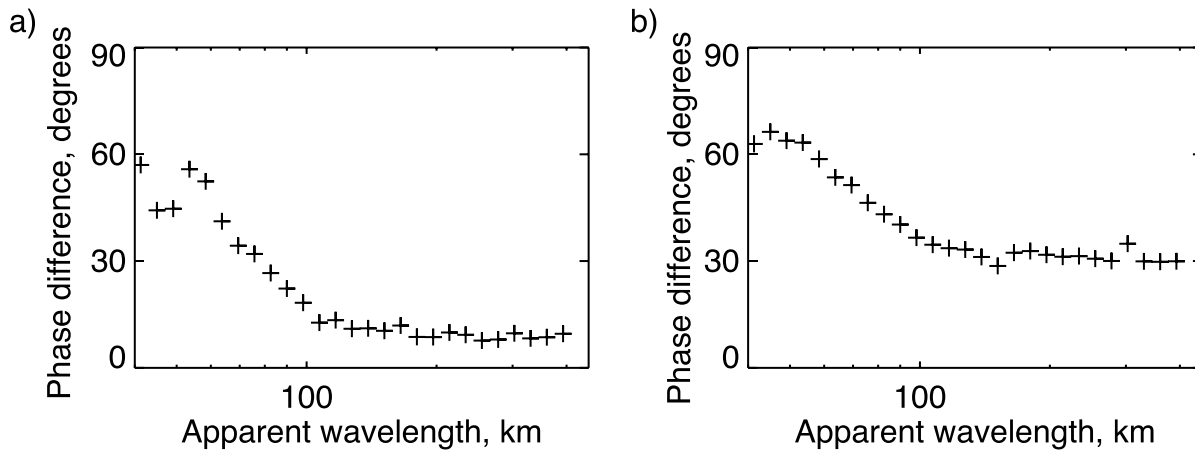


Figure 9. Difference in the phase of the waves observed in CO₂ to that observed in (a) Ar and (b) N₂ as a function of apparent wavelength as defined the text. Values are computed from all measurements taken in May 2015 below ~205 km altitude above the areoid and above 5 km from periapsis, as described in section 4.1.

4.6. Changes in Observed Amplitude With Altitude

Assuming the same latitudes and local times are sampled at each altitude, which is effectively the case for a 1 month average of NGIMS data (see Figure 2), examining the wave amplitude as a function of altitude provides information on the vertical propagation of the waves. In the absence of any sources of waves or dissipation, the wave amplitudes are expected to grow exponentially with altitude as the atmospheric density decreases [e.g., Hines, 1960]. Further, as H_i is species-dependent, it is expected that this vertical growth rate will vary by species. Figure 10 shows the mean value of $\rho' / \bar{\rho}$ as a function of altitude for CO₂ and N₂, averaged over all values for May 2015. Given that H_{CO_2} is 13.4 km and H_{N_2} is 21.0 km, the growth in $\rho' / \bar{\rho}$ over the 40 km altitude range shown would be a factor of 4.4 for CO₂ and a factor of 2.6 for N₂, in the absence of any dissipation. This is clearly not the case, and the observations shown in Figure 10 suggest that the amplitude of the waves is limited by dissipation at these altitudes, which is consistent with the NGIMS observations of small-scale waves during December 2014 reported by Yigit *et al.* [2015a] and may indicate processes such as wave saturation or viscous dissipation that are limiting the wave growth with altitude. Using the NGIMS observations of Ar densities, Terada *et al.* [2017] have shown that wave saturation likely limits the growth of gravity waves in the altitude region considered here, which is consistent with the result shown in Figure 10. Given the observations shown in

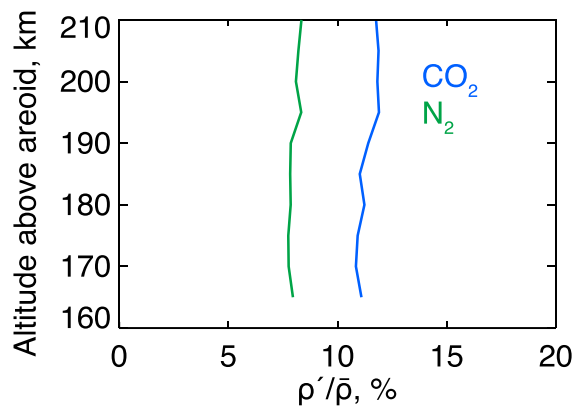


Figure 10. Average values of $\rho' / \bar{\rho}$ for CO₂ and N₂ as functions of altitude for all data taken during May 2015. Values are shown for 5 km altitude bins.

Figure 10, and the values of H_i for each species, it is possible to calculate a scale length associated with this dissipation, given by

$$\frac{\rho'_i}{\bar{\rho}_i} \propto \left[\left(\frac{1}{2H_i} - \frac{1}{K_{z,i}} \right) z \right], \quad (2)$$

where $K_{z,i}$ is the decay-scale length and varies by species [e.g., Cui *et al.*, 2014]. Using equation (2) and the observed values of H_i and $\rho'_i/\bar{\rho}_i$ as a function of altitude, we find $K_{zCO_2} = 38$ km and $K_{zN_2} = 61$ km for this case. The values of $K_{z,i}$ are similar to those of $2H_i$, which corresponds to the near balance of growth and dissipation in this region.

5. Monthly Mean Observed Properties

Using the data taken with the NGIMS instrument over several months, it is possible to study how the properties of the waves and background atmosphere change as the MAVEN spacecraft's periapsis moves in latitude and local time. The effect of orbital evolution on the sampling of the NGIMS instrument can be seen in Figure 2. As the periapsis of the spacecraft moves in latitude and local time, the MAVEN spacecraft adjusts the altitude of periapsis to target a mean periapsis density of 0.05–0.15 kg/km³ [Jakosky *et al.*, 2015]. In addition, during periodic campaigns referred to as Deep Dips [Bougher *et al.*, 2015], the periapsis altitude is decreased by several tens of kilometers for several orbits (see Figure 2). To be able to compare the data taken in different months and identify trends with latitude or local time, we must therefore take into consideration these changes in the orbit geometry. Comparing data at the same altitudes can be done, but only at the highest altitude sampled (approximately the 170–205 km region), where the densities are low (especially on the nightside) and as such the signal-to-noise ratio for certain species becomes lower than desired. Further, at the top of this altitude range, the density of O can sometimes exceed that of CO₂ on the nightside, which will significantly complicate the analysis presented in section 6. Comparing data at the same range of atmospheric pressure would perhaps be ideal, but owing to a combination of the MAVEN orbit targeting a fixed atmospheric density and the significant day to night temperature difference in the Martian thermosphere, only a very small amount of the data observed in the ~170–205 km altitude region through the MAVEN mission correspond to the same atmospheric pressure range. Given that the MAVEN spacecraft orbit changes in response to atmospheric density, it is possible to use a fixed density range in order to compare observations from different months. By selecting an altitude range corresponding to monthly mean CO₂ densities from 1.5×10^9 cm⁻³ to 1.5×10^8 cm⁻³, the same density corridor can be compared in each month, and the analysis can focus on a region where the noise level is extremely low and the CO₂ is always the dominant species.

As in section 4, using approximately 1 month of data provides a sufficient number of orbits for the mean properties of the waves as functions of apparent wavelength and the background atmosphere to be found, and yet the NGIMS observations span a fairly limited range of latitudes and local time (periapsis motion is typically 30° latitude and 2 h of local time; see Figure 2). All data from February 2015 to March 2016 have been divided into the ~1 month segments, highlighted in Figure 2. As the data available begin on 17 February 2015, the data from February and the first half of March are grouped into 1 month. As a significant number of orbits from April 2015 are missing, the data from the second half of March and April are grouped into 1 month. Finally, note that there are no data available from June 2015. For each of the months listed, we determine the background atmosphere in terms of temperature (T), the range in the total atmospheric pressure (p), density for each major species (ρ_i), and the scale-height for each major species (H_i). These are shown in Table 1 for each month included in this study.

All wave parameters described in section 4 are also found as functions of apparent wavelength. To identify a characteristic value of each parameter, rather than taking a simple mean of all values, we find the mean for apparent wavelengths of 90 km and longer, for which the values of $\rho'_i/\bar{\rho}_i$ are unaffected by the instrumental noise (see Figure 7), and for which the phase and amplitude ratios between minor and major species are approximately constant (see Figure 9). Table 2 summarizes these observed wave parameters.

Examining Tables 1 and 2, we can see that on several occasions the same latitude region is sampled in more than 1 month. Comparing May 2015 ($L_s = 341^\circ$, just prior to equinox) with November 2015 ($L_s = 95^\circ$, northern

Table 1. Mean Observed Atmospheric Properties^a

Date Range (dd/mm/yy)	Altitude Range (km)	L_s (deg)	Latitude (deg)	Local Time (h)	T (K)	$P_{total,r}$ Range (N/m ²)	$\rho_{total,r}$ (g/cm ³)	Buoyancy Period (min)	Scale Height (km)				
									CO ₂	Ar	N ₂	CO	O
11/02/15 to 15/03/15	167–200	300	29	16.5	241	7.0e–6 to 1.0 e–6	4.5e-11	6.9	14.2	16.2	21.6	19.7	27.8
16/03/15 to 30/04/15	177–211	318	6.5	13.3	268	7.6e–6 to 1.0 e–6	4.4e-11	6.8	14.5	15.5	20.0	16.8	25.8
01/05/15 to 26/05/15	168–204	341	-21	9.7	241	6.8e–6 to 9.3e–7	4.4e-11	7.2	16.0	17.7	24.3	20.4	29.2
02/07/15 to 31/07/15	151–170	13	-65	6.1*	142	4.9e–6 to 8.2e–7	5.4e-11	5.3	8.1	9.2	12.6	9.0	22.8
01/08/15 to 31/08/15	150–174	27	-70	16.7*	152	4.6e–6 to 7.4e–7	4.8e-11	6.0	10.4	12.0	15.8	14.7	22.8
02/09/15 to 30/09/15	157–185	42	-56	14.9	194	6.1e–6 to 8.1e–7	4.7e-11	6.2	12.0	14.1	19.3	10.9	25.5
01/10/15 to 31/10/15	157–184	55	-37	11.5	209	6.0e–6 to 8.9e–7	4.5e-11	6.2	11.6	13.6	18.8	15.2	23.5
01/11/15 to 30/11/15	154–178	68	-16	8.9	192	5.7e–6 to 9.4e–7	4.7e-11	6.1	10.7	12.7	17.9	14.4	26.2
01/12/15 to 31/12/15	147–170	82	5.4	6.2	179	5.3e–6 to 8.3e–7	4.6e-11	5.8	10.1	12.1	16.0	14.3	22.7
01/01/16 to 31/01/16	145–167	95	29	3.1	155	4.3e–6 to 6.4e–7	4.4e-11	5.6	9.5	11.3	15.3	14.7	19.4
01/02/16 to 29/02/16	152–179	109	51	12.8	184	5.3e–6 to 7.6e–7	4.5e-11	6.2	11.7	13.6	18.2	15.6	22.3
01/03/16 to 31/03/16	160–190	123	68	19.2*	199	5.9e–6 to 8.7e–7	4.6e-11	6.5	12.9	14.9	20.2	16.4	23.8

^aThe dates corresponding to each approximately 1 month grouping of data are shown in Figure 2. Note that the local time for certain months, denoted by the star, spans a wide range.

hemisphere summer), we see that both sets of observations correspond to approximately the same latitude and local time, and thus, the main differences seen between these two can be attributed to changes in season. During both May and November 2015, the observations are centered around low latitudes, just south of the equator. The higher temperature, scale heights, and altitude range sampled in May compared to November are consistent with Mars being close to aphelion in November. The smaller scale heights observed during November may be expected to correspond to larger wave amplitudes (section 4.2), but approximately, the same relative amplitude in density and temperature is seen in both months, which may be a result of differences in the season producing different forcing or filtering of atmospheric waves. Comparing March 2015 with December 2015 or February 2015 with January 2016, the observations taken in each pair of months correspond to both changes in season and local time. Notably, February and March are daytime (16.5 and 13.3 h, respectively), whereas December is near the terminator and January is during the nighttime (6.2 and 3.1 h, respectively). As may be expected, the altitude ranges sampled, background temperatures, and species scale heights are all significantly lower during December and January compared with March and February. Correspondingly, the wave amplitudes observed during December and January are more than double those seen in March and February. It is not possible to determine if these are seasonal or local time effects, but such changes would be expected from local time variations alone, and are consistent with the results of *Yiğit et al.* [2015a].

Table 2. Mean Observed Wave Properties as Defined in the Text^a

Date Range (dd/mm/yy)	$\frac{\rho_{CO_2}}{\rho_{CO_2}}$ (%)	T (K)	K_{zj} (km)			Relative Amplitude N ₂ /CO ₂	Phase Difference CO ₂ :N ₂ (deg)
			CO ₂	Ar	N ₂		
11/02/15 to 15/03/15	8	15	26	30	40	0.7	34
16/03/15 to 30/04/15	8	17	28	33	52	0.7	37
01/05/15 to 26/05/15	11	17	38	44	61	0.7	32
02/07/15 to 31/07/15	22	27	18	21	21	0.7	29
01/08/15 to 31/08/15	18	22	20	23	25	0.7	29
02/09/15 to 30/09/15	12	19	15	17	19	0.7	34
01/10/15 to 31/10/15	11	18	23	26	31	0.7	33
01/11/15 to 30/11/15	11	16	22	25	30	0.7	31
01/12/15 to 31/12/15	15	21	16	18	21	0.7	31
01/01/16 to 31/01/16	21	27	14	16	17	0.7	28
01/02/16 to 29/02/16	19	31	21	24	28	0.7	28
01/03/16 to 31/03/16	7	21	29	40	53	0.7	34

^aThe dates corresponding to each approximately 1 month grouping of data are shown in Figure 2.

6. Estimating Intrinsic Wave Parameters and Heating Rates

As discussed in section 4.3, the apparent wavelength is only a proxy for the intrinsic wavelength of any wave seen. From in situ measurements of density alone, it is not possible to determine the angle between the spacecraft velocity and the wave phase velocity and so it is impossible to quantitatively determine the wave parameters. However, several previous studies have used mass spectrometer observations of multiple atmospheric species, along with a model of the phase and amplitude differences between species, to provide constraints on the intrinsic properties of the waves observed [e.g., *Dudis and Reber, 1976; Del Genio et al., 1978, 1979; Cui et al., 2013, 2014*]. Following the overall approach of *Cui et al. [2014]*, in this section we will use a linearized, two-fluid approximation of internal waves to identify the properties and nature of an internal wave that provides the best fit to the observed wave properties listed in Table 2.

6.1. Constraints From Wave Decay Scale Lengths

The decay scale length, K_{zi} , is expected to vary with the properties of the wave, such as its wavelength and frequency. Using such a theoretical relationship for the decay scale length, and the observations summarized in Table 2, it is therefore possible to provide some constraint on the properties of the waves observed.

Cui et al. [2014] showed that if diffusion is slow and viscosity dominates the wave damping, then for inertial gravity waves the ratio of the decay scale lengths between different species is proportional to the ratio of η_i/H_i^2 , where η_i is the kinematic viscosity. Similarly, for acoustic-gravity waves, the ratio of the decay scale lengths is proportional to the ratio of η_i . If diffusion is fast, then binary diffusion dominates the decay of atmospheric waves. In this case, the ratios of the decay scale lengths for inertial and acoustic-gravity waves given by *Cui et al. [2014]* are proportional to the ratios of v_{ij}/H_i and v_{ij} , respectively, where v_{ij} is the binary collision frequency. During May 2015, the observed ratio of decay scale lengths for CO₂:Ar and CO₂:N₂ were 0.86 and 0.62. Using the above theoretical ratios, the observed atmospheric properties given in Table 1, and the formulation for kinematic viscosity and binary diffusion from *Cui et al. [2014]*, the theoretical ratios for inertial gravity waves in the slow diffusion case are 0.76 and 0.68, for CO₂:Ar and CO₂:N₂, and in the fast diffusion case are 3.9 and 3.3. Similarly, for acoustic-gravity waves in the slow diffusion case the theoretical ratios are 0.94 and 1.6 and in the fast diffusion case are 4.3 and 4.9. The inertial gravity wave, slow diffusion case matches the observed ratio well, which agrees with the findings discussed in sections 4.2 and 4.4. In this case, *Cui et al. [2014]* gives the theoretical relationship of the decay scale length to the wave properties as

$$K_{zi} \approx \frac{\omega k^2 (k^2 + 1/4H_i^2)}{(\omega^2 - f^2) |k_z|} \eta_i, \quad (3)$$

where f is the Coriolis frequency, k_z is the vertical wave number, and k is the total wave number ($(k_h^2 + k_z^2)^{1/2}$). The wave frequency is related to the horizontal and vertical wave numbers (k_h and k_z , respectively) via the dispersion relation, which for inertial gravity waves is given by

$$\omega^2 = \frac{N_B^2 k_h^2 + f^2 (k_z^2 + 1/4H_i^2)}{k_h^2 + k_z^2 + 1/4H_i^2}, \quad (4)$$

where N_B is Brunt-Väisälä frequency, given by

$$N_B^2 = \frac{g}{T} \left(\frac{dT}{dz} + \frac{g}{c_p} \right), \quad (5)$$

where g is the acceleration due to gravity and c_p is the specific heat capacity at constant pressure, and for acoustic-gravity waves by

$$\omega^2 = c_i^2 (k_z^2 + 1/4H_i^2), \quad (6)$$

where c_i is the sound speed. Combining equations (3)–(6) provides a means of relating an observed quantity (K_{zi}), to the horizontal and vertical wavelength of the wave, which cannot be directly observed by NGIMS. This, along with other constraints, will be used to find a wave that fits the observed properties in section 6.3.

6.2. The Two-Fluid Linear Model

Previous studies [e.g., *Del Genio et al., 1979; Cui et al., 2013, 2014*] have used two-fluid linear wave models to infer atmospheric wave properties based on the observed phase and amplitude differences between the

major and minor species. Following the formulation presented by Cui *et al.* [2013], plane wave solutions of the form

$$\exp\left(\frac{z}{2H_i}\right) \exp(i[\omega t, k_h x, k_z z]), \quad (7)$$

are sought to the linearized fluid equations. For the case of CO₂ as the major species, the equations of continuity, horizontal and vertical momentum, and energy are

$$i\omega \frac{\tilde{\rho}_{\text{CO}_2}}{\bar{\rho}_{\text{CO}_2}} - ik_h \tilde{u}_{\text{CO}_2} - \left(\frac{1}{2H_{\text{CO}_2}} + ik_z\right) \tilde{w}_{\text{CO}_2} = 0, \quad (8)$$

$$i\omega \tilde{u}_{\text{CO}_2} - \frac{ik_h}{\gamma_{\text{CO}_2}} c_{\text{CO}_2}^2 \frac{\tilde{\rho}_{\text{CO}_2}}{\bar{\rho}_{\text{CO}_2}} = 0, \quad (9)$$

$$i\omega \tilde{w}_{\text{CO}_2} - \left(\frac{1}{2H_{\text{CO}_2}} + ik_z\right) c_{\text{CO}_2}^2 \frac{\tilde{\rho}_{\text{CO}_2}}{\bar{\rho}_{\text{CO}_2}} + \frac{\tilde{\rho}_{\text{CO}_2}}{\bar{\rho}_{\text{CO}_2}} g = 0, \quad (10)$$

and

$$i\omega \frac{\tilde{\rho}_{\text{CO}_2}}{\bar{\rho}_{\text{CO}_2}} - \frac{\tilde{w}_{\text{CO}_2}}{H_{\text{CO}_2}} = \gamma_{\text{CO}_2} \left(i\omega \frac{\tilde{\rho}_{\text{CO}_2}}{\bar{\rho}_{\text{CO}_2}} - \frac{\tilde{w}_{\text{CO}_2}}{H_{\text{CO}_2}} \right), \quad (11)$$

where u is the horizontal velocity, w is the vertical velocity, g is the acceleration due to gravity, γ_i is the ratio of specific heats, and $\tilde{\rho}$, \tilde{p} , \tilde{u} , and \tilde{w} are the complex constants of the polarization relations [Hines, 1960].

For the minor species, collisions with the major species mean that wave-induced diffusion can be important on the time scale of the waves [e.g., Del Genio *et al.*, 1978, 1979], and therefore, this should be included in the fluid equations. For the case of N₂ as the minor species, the fluid equations are given by

$$i\omega \frac{\tilde{\rho}_{\text{N}_2}}{\bar{\rho}_{\text{N}_2}} - ik_h \tilde{u}_{\text{N}_2} - \left(\frac{1}{2H_{\text{N}_2}} + ik_z\right) \tilde{w}_{\text{N}_2} = 0, \quad (12)$$

$$i\omega \tilde{u}_{\text{N}_2} - \frac{ik_h}{\gamma_{\text{N}_2}} c_{\text{N}_2}^2 \frac{\tilde{\rho}_{\text{N}_2}}{\bar{\rho}_{\text{N}_2}} = -v_{\text{N}_2\text{CO}_2} (\tilde{u}_{\text{N}_2} - \tilde{u}_{\text{CO}_2}), \quad (13)$$

$$i\omega \tilde{w}_{\text{N}_2} - \left(\frac{1}{2H_{\text{N}_2}} + ik_z\right) c_{\text{N}_2}^2 \frac{\tilde{\rho}_{\text{N}_2}}{\bar{\rho}_{\text{N}_2}} + \frac{\tilde{\rho}_{\text{N}_2}}{\bar{\rho}_{\text{N}_2}} g = -v_{\text{N}_2\text{CO}_2} (\tilde{w}_{\text{N}_2} - \tilde{w}_{\text{CO}_2}), \quad (14)$$

and

$$i\omega \frac{\tilde{\rho}_{\text{N}_2}}{\bar{\rho}_{\text{N}_2}} - \frac{\tilde{w}_{\text{N}_2}}{H_{\text{N}_2}} = \gamma_{\text{N}_2} \left(i\omega \frac{\tilde{\rho}_{\text{N}_2}}{\bar{\rho}_{\text{N}_2}} - \frac{\tilde{w}_{\text{N}_2}}{H_{\text{N}_2}} \right). \quad (15)$$

For the formulation given by equations (8)–(15) to be used, it is important that one species be significantly more abundant than all others over the altitude range considered. For the density range selected for this study, CO₂ is always the dominant species. Equations (8)–(15) can therefore be solved for $(\tilde{\rho}_{\text{N}_2}/\bar{\rho}_{\text{N}_2})/(\tilde{\rho}_{\text{CO}_2}/\bar{\rho}_{\text{CO}_2})$, the real part of which gives the relative amplitude ratio and the complex part of which gives the phase difference. Thus, the solution to these equations allows us to use two other observed quantities to provide constraints on the properties of the observed waves. Note that the solution for $(\tilde{\rho}_{\text{N}_2}/\bar{\rho}_{\text{N}_2})/(\tilde{\rho}_{\text{CO}_2}/\bar{\rho}_{\text{CO}_2})$ is found for the averaged observed properties over the region of interest, and the atmospheric and wave properties are found for the mean value within that range (i.e., no variation in altitude is included in the calculation).

6.3. Determination of the Most Characteristic Wave

Cui *et al.* [2014] used the observed values of K_{zj} and $\tilde{\rho}_i/\tilde{\rho}_j$ at Titan, along with the two-fluid model described above, to search for gravity wave parameters that are best able to account for those observed quantities. Here we adapt this approach for use with the NGIMS observations at Mars. At Titan, the dominant species in the upper atmosphere is N₂, which has a significantly different scale height to the dominant minor species, CH₄. For the minor species ²⁹N₂, which has an almost identical scale height to ²⁸N₂, the observed relative amplitude ratio did not prove to be a useful constraint [Cui *et al.*, 2014, Figure 17]. Considering the observations from NGIMS at Mars, CO₂ is the dominant species at all altitudes considered here. Ar is observed on every orbit but has a very similar scale height to CO₂, and only a very small phase and amplitude difference

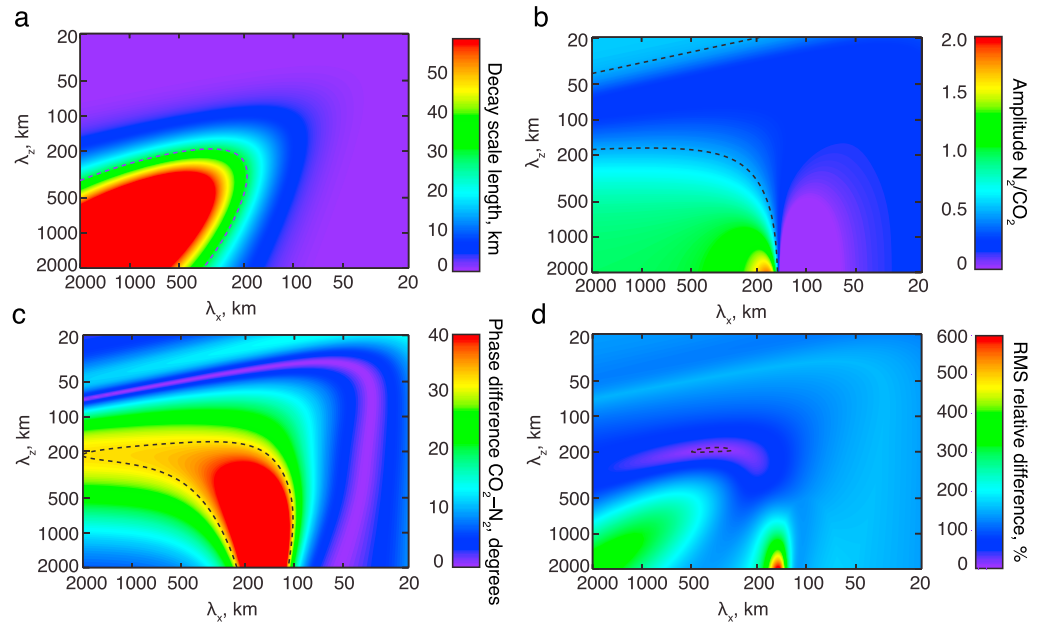


Figure 11. (a) The computed values of the decay scale length for perturbations in CO₂ density as described in the text, as functions of the horizontal and vertical wavelengths of the inertial gravity wave selected. The values correspond to the observed decay scale length are marked by the dashed black line. All values are for NGIMS observations during May 2015. (b) As Figure 11a but for the ratio of the amplitude of density perturbations in CO₂ to N₂. (c) As Figure 11a but for the phase difference in the density perturbations in CO₂ to N₂. (d) The route-mean-square of the relative difference between the observed and theoretical values of the three quantities shown in Figures 11a through 11c. The dashed black line marks the region of 10% RMS relative difference. The minimum value is 6% for $\lambda_x = 370$ km and $\lambda_z = 190$ km.

is seen between these two. Therefore, we will use the observed differences between CO₂ and N₂, and K_{zCO_2} . One additional constraint is also required, so here we will use the observed phase difference between CO₂ and N₂.

The values of H_i , N_B , viscosity, and binary collision frequency are determined from the NGIMS observations summarized in Table 1, using the formulation from Cui *et al.* [2014, Appendix B]. Using these, for any given horizontal and vertical wavelength (λ_x, λ_z) chosen, the corresponding wave period (ω) is found from the gravity wave dispersion relation (equation (4)). Using these wave and atmospheric properties, the theoretical value of K_{zCO_2} is calculated by using equation (3). This process is repeated for all combinations of λ_x and λ_z from 20 to 2000 km. The calculated values of K_{zCO_2} are shown in Figure 11a. The predicted decay scale lengths vary from ~ 1 km for the shortest wavelengths to several hundreds of kilometers for the very longest wavelengths, as may be expected from an examination of equation (3). The observed K_{zCO_2} of 38 km is shown with the dashed black line. As can be seen, from this condition alone, an infinite number of possible combinations of λ_x and λ_z falling along the dashed line shown could explain the observed value of K_{zCO_2} .

A similar approach is taken for the relative amplitude ratio and the phase difference between $\tilde{\rho}_{CO_2}$ and $\tilde{\rho}_{N_2}$. Here equations (8)–(14) are solved for $(\tilde{\rho}_{N_2}/\tilde{\rho}_{N_2})/(\tilde{\rho}_{CO_2}/\tilde{\rho}_{CO_2})$ in terms of ω, λ_x , and λ_z . Using a chosen combination of λ_x, λ_z , and ω from the dispersion relation, and the background atmospheric properties observed by NGIMS, the resultant complex value of $(\tilde{\rho}_{N_2}/\tilde{\rho}_{N_2})/(\tilde{\rho}_{CO_2}/\tilde{\rho}_{CO_2})$ is found, which gives both the real value of the relative amplitude ratio and the phase difference between $\tilde{\rho}_{CO_2}$ and $\tilde{\rho}_{N_2}$. Figures 11b and 11c show the calculated and observed values of these two quantities in the same format as Figure 11a.

The best fit combination of λ_x and λ_z to all three observed quantities is found from the route-mean-square (RMS) of the relative difference between the computed and observed values for each value of λ_x and λ_z . These calculated RMS values are shown for all values of λ_x and λ_z in Figure 11d. As can be seen, there is a region of minimum difference, where the calculated values come close to all three observed quantities near $\lambda_x \approx 300$ – 500 km and $\lambda_z \approx 200$ km. The minimum RMS difference is 6% for $\lambda_x = 370$ km and $\lambda_z = 190$ km. While this combination of wavelengths was calculated by using only the observed values of K_{zCO_2} , the relative

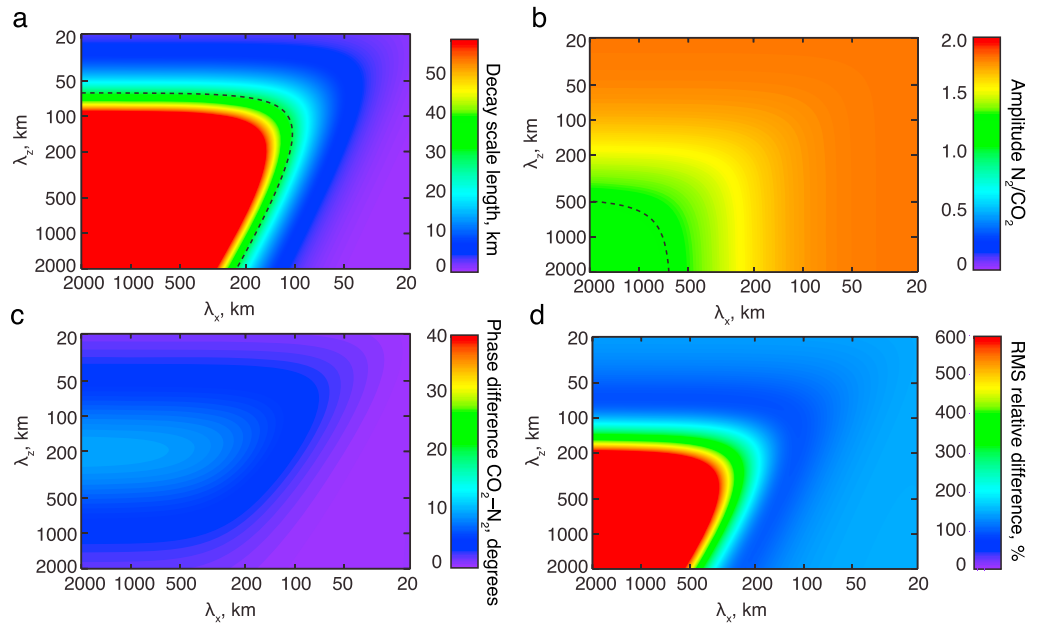


Figure 12. As Figure 11 but for the acoustic-gravity waves. The minimum RMS relative difference found is 90%.

amplitude ratio, and the phase difference between $\tilde{\rho}_{\text{CO}_2}$ and $\tilde{\rho}_{\text{N}_2}$, it fits well with the typical apparent wavelengths noted in Figure 5 (also recall that only apparent wavelengths of 90 km and above are used to determine the observed characteristics). This, along with the low value of the RMS relative difference between the computed and observed values shown in Figure 11d, provides some measure of how well the simple linear two-fluid model used here can simultaneously account for the all of these observed properties.

Finally, while inertial gravity waves are found to be the best fit to the observed ratios of K_{zi} described in section 6.1, *Walterscheid et al.* [2013] showed that acoustic-gravity waves may propagate efficiently into the upper thermosphere. Therefore, it is instructive to consider the possibility that the density perturbations observed by NGIMS in this region may be associated with acoustic-gravity waves. The same approach described above can be applied to find the best fit acoustic-gravity wave if we use the acoustic-gravity wave dispersion relation to compute ω from λ_x and λ_z , and the decay scale length is computed from

$$K_{zi} \approx \frac{\omega k^2 (k^2 + 1/4H_i^2)}{\omega^2 |k_z|} \eta_i. \tag{16}$$

Figure 12 shows the comparison of the computed values of $K_{z\text{CO}_2}$, the relative density amplitudes, and the phase difference between $\tilde{\rho}_{\text{CO}_2}$ and $\tilde{\rho}_{\text{N}_2}$ for acoustic-gravity waves to the observed values. As can be seen, while solutions exist for the observed values of $K_{z\text{CO}_2}$ and the relative density amplitudes for reasonable values of λ_x and λ_z , these do not overlap with one another. Further, it is not possible to account for the observed phase difference between $\tilde{\rho}_{\text{CO}_2}$ and $\tilde{\rho}_{\text{N}_2}$ for acoustic-gravity waves with the simple model used here. This is reflected in the computed RMS relative difference values, which show a minimum difference of 90%, which is significantly worse than the fit for inertial gravity waves. If acoustic-gravity waves are a significant portion of the spectrum at these altitudes, it is possible that these are not the primary source of the NGIMS observations or that a more sophisticated model may be needed to identify these. As such, for the remainder of our analysis, we shall assume that the waves observed by NGIMS are inertial gravity waves.

6.4. Estimation of Heating Rates

While numerous studies using first-principals models of atmospheric gravity waves have shown that these may carry a significant heat flux in the Martian thermosphere and perturb the temperature structure there [e.g., *Medvedev and Yiğit, 2012; Medvedev et al., 2015*], thus significantly impacting the thermal structure of this region, there has been no observationally based estimate of these heating rates. The analysis described

in section 6.1 provides information on the best fit values of ω , λ_x , and λ_z for the waves seen during May 2015. These, along with the observed values of the wave amplitudes, and the background atmosphere (H_i , N_B , $\bar{\rho}_i$, etc), provide all of the information required to estimate the heat flux associated with the gravity waves observed by NGIMS.

Snowden and Yelle [2014] used mass spectrometer observations at Titan to provide comparable estimates of the heating rate produced by the gravity waves observed. Following the same approach, the viscous heating rate associated with gravity waves whose amplitude is saturated (consistent with Figure 10) is given by

$$\bar{\rho}c_pQ = \frac{\mu}{H^2} \bar{\rho} \frac{g^2}{N_B^2} \left(\frac{\rho'}{\bar{\rho}} \right)^2, \quad (17)$$

where c_p is the specific heat capacity of the atmosphere, Q is the heating rate, and μ is the viscosity coefficient. The sensible heat flux (which leads to cooling in the thermosphere) for weakly damped waves, such as those seen here, is given by *Hickey et al.* [2011] as

$$\bar{\rho}c_pQ = -\frac{k_z^2 c_p \mu \bar{\rho} g^2}{RN_B^2} \left\langle \left(T' / \bar{T} \right)^2 \right\rangle, \quad (18)$$

where R is the universal gas constant. For the conditions in May 2015, the viscous heating rate is estimated to be 182 K/sol, and the sensible heat flux is estimated to be -76 K/sol, corresponding to a net heating rate of 106 K/sol in the 168–204 km altitude region. While no previously published model-based estimate of the gravity wave heating/cooling rates matches the exact season, altitude, latitude, and local time of the conditions used here, this heating/cooling rate is in broad agreement with the magnitude of estimates by a number of works, including the general circulation modeling of *Medvedev and Yiğit* [2012], and the one-dimensional numerical simulations of *Parish et al.* [2009].

It is worth noting here that the heating and cooling rates estimated in this section are based on a best fit to the mean properties of the waves observed. However, a broad spectrum of waves exists within this region (see, for example, Figure 5). Therefore, an estimate could be obtained by dividing the observed data set into ranges of apparent wavelengths, and then determining the best fit wave for each of these ranges. This could be done with the same approach outlined here but is beyond the scope of this work. Rather, in the next section, we will investigate how these heating rates vary throughout the MAVEN observations used in this study.

6.5. Monthly Variations of Derived Wave Parameters

The method for determining the most characteristic wave and estimating the gravity wave heating/cooling rate described in sections 6.3 and 6.4 is repeated for all months included in this study. The properties of the waves and estimated heating rates are summarized in Table 3. A wide range of heating rates is found, which is reflective of the variation in atmospheric conditions and wave amplitudes seen. The largest heating rate due to viscous wave damping is found during December 2015, when NGIMS samples near the dawn terminator, close to the equator. The largest cooling rate due to sensible heat flux is found during July 2015, when NGIMS samples the nightside at high southern latitudes. Note that, during July 2015, the NGIMS observations span a wide range of local times, but all are at high solar zenith angles.

To examine if any clear trends exist in the observed and estimated values in Table 3, Figure 13 shows the dependence of the wave amplitudes and heating rates on background conditions. The observed wave amplitudes ($\rho' / \bar{\rho}$) appear to be anticorrelated with the background temperature, shown in Figure 13a. As the CO_2 scale height is proportional to the background temperature, this trend is expected from equation (1) and the behavior described in section 4.2. The estimated cooling rates have a weak negative correlation with solar zenith angle, and a much clearer negative correlation with $\rho' / \bar{\rho}$ (Figures 13b and 13c). For the heating rates, these appear to have a weak positive correlation with solar zenith angle, and a slightly stronger positive correlation with $\rho' / \bar{\rho}$. Given the behavior shown in Figure 13a, this behavior is expected from equations (17) and (18), if variations in the vertical wavelength and other parameters between different months are of secondary importance. The net heating rates are shown in Figure 13d as a function of latitude and solar zenith angle. For each, the solar longitude is noted. There are only 2 months in which there is net cooling, both of which occur at mid-high southern latitudes and occur just after equinox. One of these, September 2015 includes observations prior to sunset, while July 2015 includes observations from the nightside. It is worth noting that for the

Table 3. Properties of the Gravity Waves, Inferred From the Best Fits to the Linear Two-Fluid Model Described in the Text^a

Date Range (dd/mm/yy)	Latitude (deg)	Local time (h)	Solar Zenith Angle (deg)	$\frac{\rho_{CO_2}}{\rho_{CO_2}}$ (%)	Best Fit λ_x, λ_z (km)	Heating Rate due to Viscous Damping, Sensible Heat Flux (K/sol)
11/02/15 to 15/03/15	29	16.5	82	8	590, 180	74, -60
16/03/15 to 30/04/15	6.5	13.3	23	8	440, 180	120, -65
01/05/15 to 26/05/15	-21	9.7	56	11	370, 190	182, -76
02/07/15 to 31/07/15	-65	6.1*	110	22	770, 150	447, -586
01/08/15 to 31/08/15	-70	16.7*	100	18	770, 160	401, -336
02/09/15 to 30/09/15	-56	14.9	83	12	1000, 170	102, -163
01/10/15 to 31/10/15	-37	11.5	52	11	670, 170	187, -113
01/11/15 to 30/11/15	-16	8.9	53	11	830, 180	270, -94
01/12/15 to 31/12/15	5.4	6.2	87	15	1110, 170	639, -205
01/01/16 to 31/01/16	29	3.1	130	21	1430, 170	483, -411
01/02/16 to 29/02/16	51	12.8	60	19	830, 170	602, -414
01/03/16 to 31/03/16	68	19.2*	110	7	630, 190	308, -140

^aThe dates corresponding to each approximately 1 month grouping of data are shown in Figure 2. Note that the local time for certain months, denoted by the star, spans a wide range.

third set of observations to occur in this same latitude region, August 2015, only a small net heating is found. More observations would be required to determine if the net cooling rates found in this region are a result of the gravity wave forcing at these latitudes or are a result of the seasonal and solar zenith angle conditions. The largest net heating rates are found in two regions, first at low latitudes for solar zenith angles from ~ 45 to 90° , and at northern latitudes above 45° . The strong heating rates near the equator occur at a range of solar longitudes from equinox through northern hemisphere summer, while the observations at high northern latitudes correspond to northern hemisphere summer. Several other samples, in the same range of solar longitudes and at northern low latitude and midlatitude, do not show strong net heating, which again makes it difficult to determine if a single factor controls this.

It is instructive to compare the pairs of months considered in section 5. Comparing May 2015 with November 2015, both months include data from low latitudes, just south of the equator and the same around 9 h local time. The amplitude of the waves seen in both months are similar, and while there is a significant difference in the best fit values of λ_x , the best fit values of λ_z are similar. A strong net positive heating rate (over 100 K/sol) is found in both cases. Comparing March 2015 and December 2015, both months include data from just north of the equator, but the March data correspond to just after midday, whereas the December data correspond to near sunrise. The wave amplitudes observed during December are significantly larger than those seen in March, which may be a result of the different background thermal structure and differences in the GW propagation and dissipation characteristics. Again, there is a significant difference in the best fit values of λ_x , but similarity in the best fit values of λ_z . While a net heating is seen in both months, it is substantially stronger in December. Comparing February 2015 with January 2016, both months include data from around 29° north, but February corresponds to presunset, whereas January corresponds to postmidnight. The wave amplitudes seen in January are significantly higher than in February, in a manner similar to March and December. Again, there is a significant difference in the best fit values of λ_x , but similarity in the best fit values of λ_z . A small net heating rate is seen in both cases. From the data considered here, no clear single factor (local time or solar longitude) seems to govern the net heating rate, although it is worth noting that the May and November compare very favorably, suggesting that at least for this case, the difference in solar longitude does not appear to have a substantial impact on the net heating rate.

While none of the model-based estimates of the gravity wave-induced heating rates discussed in section 1 were performed for the same set of conditions as the observations described in this study, the simulations of Parish *et al.* [2009] did include the same altitude region (approximately 145–210 km). Parish *et al.* [2009] simulated the effects of a wave with $\lambda_x = 150$ km, which is comparable to the best fit values shown in Table 3. However, the simulation of Parish *et al.* [2009] was performed at 82° north, which is beyond the region sampled by NGIMS and for winter solstice (hence, high solar-zenith angle). For these conditions, Parish *et al.* [2009] estimated a wave amplitude from ~ 5 to 15% in this altitude region, and a net cooling rate of ~ 50 –300 K/sol. This wave amplitude is comparable to, but slightly smaller than that typically found by NGIMS at high solar zenith angles. The range of net cooling rates estimated by Parish *et al.* [2009] over the

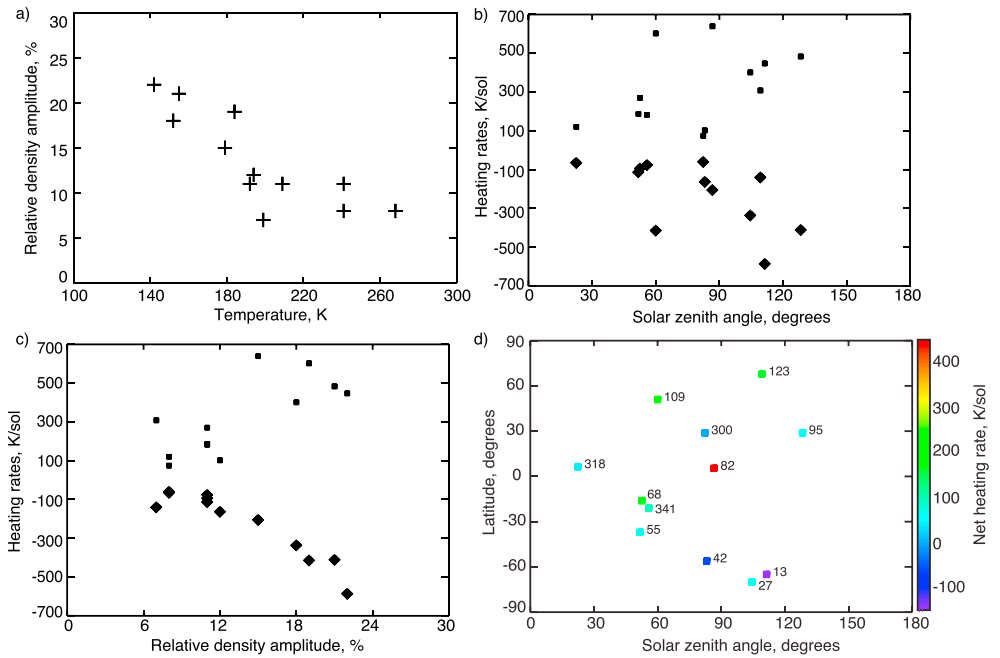


Figure 13. Scatterplots of the observed and estimated wave parameters and heating rates. (a) The relative density amplitude observed in CO₂ as a function of background atmospheric temperature, for each month shown in Table 3. (b) The estimated heating rates resulting from viscous damping (dot symbols) and from sensible heat flux (diamonds) as a function of solar zenith angle. (c) The same as Figure 13b but as a function of relative density amplitude observed in CO₂. (d) The net heating rate (color of the dot symbol) and solar longitude (number) for each month shown in Table 3 as a function of latitude and solar zenith angle.

145–211 km altitude region is comparable to the largest net cooling rates estimated here. Further, it is worth noting that while the altitudes included here are generally above those simulated by Medvedev *et al.* [2015], this study did note a complex spatial patterns in the gravity wave-induced heating and cooling, which is consistent with the results presented here. While no direct comparison can be performed yet, it would be instructive to perform such model-based estimates for the same conditions described in this work.

It is instructive to compare the estimated GW-induced heating and cooling rates to other key heating processes at these altitudes. Bougher *et al.* [2006] have computed the heating rate in the 150–170 km altitude region due to dynamic heating from thermal conduction, wind advection, and adiabatic processes by using the Mars Thermosphere General Circulation Model-MGCM coupled model and found these to be ~100–400 K/d, which is comparable to the GW-induced heating rates estimated here. On the dayside, where heating from solar EUV is also present, which is typically a factor of 3–5 higher than the dynamical or GW-induced heating rates. While a more detailed comparison between the observationally derived heating estimates and model-based estimates is clearly needed, these results suggest that heating and cooling resulting from GWs in the Martian upper thermosphere are significant, especially at night when solar EUV heating is absent.

7. Conclusions

Using neutral species measurements by Neutral Gas Ion Mass Spectrometer (NGIMS) instrument onboard NASA’s Mars Atmosphere Volatile Evolution (MAVEN) spacecraft, we have investigated wave-like signatures in the observed CO₂, N₂, and Ar densities, based on data taken from February 2015 to March 2016. By selecting an altitude range corresponding to monthly mean CO₂ densities from 1.5 × 10⁹ cm⁻³ to 1.5 × 10⁸ cm⁻³, the same density corridor can be compared for all months of data included in this study. This altitude range varies by month between 145 and 211 km. Using specific information from the wave density perturbations (relative density amplitude, wave phase, and vertical decay-scale lengths) seen in CO₂, N₂, and Ar, we have examined differences in the observations of the waves in species of different scale heights and estimate the intrinsic properties of the waves. The main findings of our study are as follows:

1. The monthly mean amplitude of the wave perturbations seen in CO₂ range from 7 to 22% in this region. Typical apparent wavelengths (seen along the orbit track) range from tens to hundreds of kilometers.
2. The relative density perturbation amplitude is seen to be anticorrelated with the background temperature, resulting in a clear day-night variation in the amplitude of the waves observed.
3. The relative density perturbation amplitudes are approximately constant as a function of altitude over the range selected, which is characteristic of waves propagating through a region of moderate damping.
4. Using information from the wave density perturbations (relative density amplitude, wave phase, and vertical decay scale lengths) seen in CO₂, N₂, and Ar, we examine differences in the observations of the waves in species of different scale heights and estimate the intrinsic properties of the waves.
5. The observed power spectral density of the temperature and density perturbations as functions of apparent wavelength, the ratio of the relative density amplitudes, the difference in the vertical decay scale lengths, and the ratio of the amplitude of the density perturbations with apparent wavelength are all consistent with relatively long-wavelength gravity waves being the cause of the density perturbations observed.
6. Using a two-fluid linear wave model in which CO₂ is treated as the dominant species and N₂ as a minor species, we determine the intrinsic wave parameters that provide the best fit to the monthly mean observed wave and background properties. These best fit parameters are able to account for the observed properties very well in the upper thermospheric region considered here.
7. From the observed properties of the background atmosphere, the amplitude of the waves, and the best fit intrinsic wave parameters, we perform the first observationally based estimate the heating rate of the Martian upper thermosphere resulting from the viscous heat flux and sensible heat flux associated with the gravity waves observed.
8. Our estimated heating rates associated with viscous heating show a weak positive correlation with both wave amplitude and solar zenith angle, whereas the cooling rates associated with sensible heat flux show a clearer negative correlation with these parameters.
9. The NGIMS observations for March 2015 and November 2015 correspond to approximately the same latitude and local time, but for different solar longitudes. In this region, we see similar wave amplitudes and estimate similar net heating rates. As additional observations are made and other regions of the planet are revisited in this manner, some clear relationships between the wave amplitudes, atmospheric heating rates, and location on the planet, season, and local time may be found.
10. Finally, our estimated GW thermal effects provide the first observational evidence that gravity wave induced heating/cooling may significantly affect the thermal structure of the Martian thermosphere, as was initially predicted by the general circulation modeling study of *Medvedev and Yiğit* [2012]. In fact, *Medvedev and Yiğit* [2012] have demonstrated that self-consistently accounting for the GW heating/cooling helps to bring the simulated temperatures by the Martian general circulation model in an excellent agreement with the ODY aerobraking temperature retrievals performed by *Bougher et al.* [2006]. Recently, the subsequent modeling of *Yiğit et al.* [2015b] showed that GWs facilitate CO₂ ice cloud formation in the lower thermosphere of Mars by cooling the atmosphere there, which further highlights the importance of GWs for the thermal balance in the Martian atmosphere. Our observational analysis suggests that in order to better understand the Martian upper atmosphere GW thermal effects should be considered in the energy budget studies of the Martian thermosphere.

Acknowledgments

All data used in the study are archived in the Planetary Atmospheres Node of the Planetary Data System (<http://pds.nasa.gov>). S.L.E., G.L., and E.Y. were supported by NASA through grant NNX13AO36G. The MAVEN mission has been funded by NASA through the Mars Exploration Program.

References

- Altieri, F., A. Spiga, L. Zasova, G. Bellucci, and J.-P. Bibring (2012), Gravity waves mapped by the OMEGA/MEX instrument through O₂ dayglow at 1.27 mm: Data analysis and atmospheric modeling, *J. Geophys. Res.*, *117*, E00J08, doi:10.1029/2012JE004065.
- Bougher, S., et al. (2015), Early MAVEN Deep Dip campaign reveals thermosphere and ionosphere variability, *Science*, *350*(6261), doi:10.1126/science.1254459.
- Bougher, S. W., J. M. Bell, J. R. Murphy, M. A. Lopez-Valverde, and P. G. Withers (2006), Polar warming in the Mars thermosphere: Seasonal variations owing to changing insolation and dust distributions, *Geophys. Res. Lett.*, *33*, L02203, doi:10.1029/2005GL024059.
- Creasey, J. E., J. M. Forbes, and G. M. Keating (2006), Density variability at scales typical of gravity waves observed in Mars' thermosphere by the MGS accelerometer, *Geophys. Res. Lett.*, *33*, L22814, doi:10.1029/2006GL027583.
- Cui, J., Y. Lian, and I. C. F. Müller-Wodarg (2013), Compositional effects in Titan's thermospheric gravity waves, *Geophys. Res. Lett.*, *40*, 43–47, doi:10.1029/2012GL054621.
- Cui, J., R. V. Yelle, T. Li, D. S. Snowden, and I. C. F. Müller-Wodarg (2014), Density waves in Titan's upper atmosphere, *J. Geophys. Res. Space Physics*, *119*, 490–518, doi:10.1002/2013JA019113.
- Del Genio, A. D., J. M. Straus, and G. Schubert (1978), Effects of wave-induced diffusion on thermospheric acoustic-gravity waves, *Geophys. Res. Lett.*, *5*, 265–267, doi:10.1029/GL005i004p00265.

- Del Genio, A. D., G. Schubert, and J. M. Straus (1979), Characteristics of acoustic-gravity waves in a diffusively separated atmosphere, *J. Geophys. Res.*, *84*, 1865–1879, doi:10.1029/JA084iA05p01865.
- Dudis, J. J., and C. A. Reber (1976), Compositional effects in thermospheric gravity waves, *Geophys. Res. Lett.*, *3*, 727–730, doi:10.1029/GL003i012p00727.
- England, S. L., et al. (2016), Simultaneous observations of atmospheric tides from combined in situ and remote observations at Mars from the MAVEN spacecraft, *J. Geophys. Res. Planets*, *121*, 594–607, doi:10.1002/2016JE004997.
- Fritts, D. C., and M. J. Alexander (2003), Gravity wave dynamics and effects in the middle atmosphere, *Rev. Geophys.*, *41*(1), 1003, doi:10.1029/2001RG000106.
- Fritts, D. C., L. Wang, and R. H. Tolson (2006), Mean and gravity wave structures and variability in the Mars upper atmosphere inferred from Mars Global Surveyor and Mars Odyssey aerobraking densities, *J. Geophys. Res.*, *111*, A12304, doi:10.1029/2006JA011897.
- Hedin, A. E., and H. G. Mayr (1987), Characteristics of wavelike fluctuations in dynamics explorer neutral composition data, *J. Geophys. Res.*, *92*, 11,159–11,172, doi:10.1029/JA092iA10p11159.
- Hickey, M. P., R. L. Walterscheid, and G. Schubert (2011), Gravity wave heating and cooling of the thermosphere: Sensible heat flux and viscous flux of kinetic energy, *J. Geophys. Res.*, *116*, A12326, doi:10.1029/2011JA016792.
- Hines, C. O. (1960), Internal atmospheric gravity waves at ionospheric heights, *Can. J. Phys.*, *38*, 1441–1481, doi:10.1139/p60-150.
- Jakosky, B. M., et al. (2015), The Mars Atmosphere and Volatile Evolution (MAVEN) mission, *Space Sci. Rev.*, doi:10.1007/s11214-015-0139-x.
- J Jeans, J. H. (1925), *The Dynamical Theory of Gases*, 4th ed., Cambridge Univ. Press, Cambridge, U. K.
- Kasprzak, W. T., A. E. Hedin, H. G. Mayr, and H. B. Niemann (1988), Wavelike perturbations observed in the neutral thermosphere of Venus, *J. Geophys. Res.*, *93*, 11,237–11,245, doi:10.1029/JA093iA10p11237.
- Kasprzak, W. T., H. B. Niemann, A. E. Hedin, and S. W. Bougher (1993), Wave-like perturbations observed at low altitudes by the Pioneer Venus Orbiter Neutral Mass Spectrometer during orbiter entry, *Geophys. Res. Lett.*, *20*, 2755–2758, doi:10.1029/93GL02628.
- Keating, G., et al. (1998), The structure of the upper atmosphere of Mars: In situ accelerometer measurements from Mars Global Surveyor, *Science*, *279*, 1672–1676, doi:10.1126/science.279.5357.1672.
- Keating, G. M., et al. (2001), Persistent planetary-scale wave-2 and wave-3 density variations observed in Mars upper atmosphere from MGS accelerometer experiment, *Proc. Eur. Geophys. Soc.*, *78*, 229.
- Keating, G. M., et al. (2003), Brief review on the results obtained with the MGS and Mars Odyssey 2001 Accelerometer Experiments, paper presented at International Workshop: Mars Atmosphere Modeling and Observations, Inst. de Astrofis. de Andalucia, Granada, Spain, 13–15 Jan.
- Lomb, N. R. (1976), Least-squares frequency analysis of unequally spaced data, *Astrophys. Space Sci.*, *39*(2), 447–462, doi:10.1007/BF00648343.
- López-Valverde, M. A., and M. López-Puertas (1994), A non-local thermodynamic equilibrium radiative transfer model for infrared emissions in the atmosphere of Mars 1. Theoretical basis and nighttime populations of vibrational levels, *J. Geophys. Res.*, *99*, 13,093–13,115, doi:10.1029/94JE00635.
- Mahaffy, P. R., et al. (2014), The Neutral Gas and Ion Mass Spectrometer on the Mars Atmosphere and Volatile Evolution mission, *Space Sci. Rev.*, doi:10.1007/s11214-014-0091-1.
- Medvedev, A. S., and E. Yiğit (2012), Thermal effects of internal gravity waves in the Martian upper atmosphere, *Geophys. Res. Lett.*, *39*, L05201, doi:10.1029/2012GL050852.
- Medvedev, A. S., E. Yiğit, and P. Hartogh (2011a), Estimates of gravity wave drag on Mars: Indication of a possible lower thermospheric wind reversal, *Icarus*, *211*, 909–912, doi:10.1016/j.icarus.2010.10.013.
- Medvedev, A. S., E. Yiğit, P. Hartogh, and E. Becker (2011b), Influence of gravity waves on the Martian atmosphere: General circulation modeling, *J. Geophys. Res.*, *116*, E10004, doi:10.1029/2011JE003848.
- Medvedev, A. S., E. Yiğit, T. Kuroda, and P. Hartogh (2013), General circulation modeling of the Martian upper atmosphere during global dust storms, *J. Geophys. Res. Planets*, *118*, 2234–2246, doi:10.1002/2013JE004429.
- Medvedev, A. S., F. González-Galindo, E. Yiğit, A. G. Feofilov, F. Forget, and P. Hartogh (2015), Cooling of the Martian thermosphere by CO₂ radiation and gravity waves: An intercomparison study with two general circulation models, *J. Geophys. Res. Planets*, *120*, 913–927, doi:10.1002/2015JE004802.
- Medvedev, A. S., et al. (2016), Comparison of the Martian thermospheric density and temperature from IUVS/MAVEN data and general circulation modeling, *Geophys. Res. Lett.*, *43*, 3095–3104, doi:10.1002/2016GL068388.
- Melo, S. M. L., et al. (2006), Using airglow measurements to observe gravity waves in the Martian atmosphere, *Adv. Space Res.*, *38*, 730–738, doi:10.1016/j.asr.2005.08.041.
- Moudden, Y., and J. M. Forbes (2010), A new interpretation of Mars aerobraking variability: Planetary wave-tide interactions, *J. Geophys. Res.*, *115*, E09005, doi:10.1029/2009JE003542.
- Müller-Wodarg, I. C. F., R. V. Yelle, N. Borggren, and J. H. Waite (2006), Waves and horizontal structures in Titan's thermosphere, *J. Geophys. Res.*, *111*, A12315, doi:10.1029/2006JA011961.
- Parish, H. F., G. Schubert, M. P. Hickey, and R. L. Walterscheid (2009), Propagation of tropospheric gravity waves into the upper atmosphere of Mars, *Icarus*, *203*, 28–37, doi:10.1016/j.icarus.2009.04.031.
- Pettengill, G. H., and P. G. Ford (2000), Winter clouds of the north Martian polar cap, *Geophys. Res. Lett.*, *27*, 609–612, doi:10.1029/1999GL010896.
- Potter, W. E., D. C. Kayser, and K. Mauersberger (1976), Direct measurements of neutral wave characteristics in the thermosphere, *J. Geophys. Res.*, *81*, 5002–5012, doi:10.1029/JA081i028p05002.
- Reber, C. A., A. E. Hedin, D. T. Pelz, W. E. Potter, and L. H. Brace (1975), Phase and amplitude relationships of wave structure observed in the lower thermosphere, *J. Geophys. Res.*, *80*, 4576–4580, doi:10.1029/JA080i034p04576.
- Scargle, J. D. (1982), Studies in astronomical time series analysis. Part II: Statistical aspects of spectral analysis of unevenly spaced data, *Astrophys. J.*, *283*, 835–853, doi:10.1086/160554.
- Snowden, D., R. V. Yelle, J. Cui, J.-E. Wahlund, N. J. T. Edberg, and K. Ågren (2013), The thermal structure of Titan's upper atmosphere. I: Temperature profiles from Cassini INMS observations, *Icarus*, *226*, 552–582, doi:10.1016/j.icarus.2013.06.006.
- Snowden, D. S., and R. V. Yelle (2014), The thermal structure of Titan's upper atmosphere. II: Energetics, *Icarus*, *228*, 64–77, doi:10.1016/j.icarus.2013.08.027.
- Terada, N., et al. (2017), Global distribution and parameter dependences of gravity wave activity in the Martian upper thermosphere derived from MAVEN/NGIMS observations, *J. Geophys. Res. Space Physics*, *122*, doi:10.1002/2016JA023476, in press.
- Tolson, R., G. Keating, R. W. Zurek, S. W. Bougher, C. J. Justus, and D. C. Fritts (2007), Application of accelerometer data to atmospheric modeling during Mars aerobraking operations, *J. Spacecr. Rockets*, *44*, 1172–1179, doi:10.2514/1.28472.

- Tolson, R., et al. (2008), Atmospheric modeling using accelerometer data during Mars Reconnaissance Orbiter aerobraking operations, *J. Spacecr. Rockets*, 45, 3, 511–518, doi:10.2514/1.34301.
- VanZandt, T. E. (1982), A universal spectrum of buoyancy waves in the atmosphere, *Geophys. Res. Lett.*, 9, 575–578, doi:10.1029/GL009i005p00575.
- Walterscheid, R. L., M. P. Hickey, and G. Schubert (2013), Wave heating and Jeans escape in the Martian upper atmosphere, *J. Geophys. Res. Planets*, 118, 2413–2422, doi:10.1002/jgre.20164.
- Wang, L., D. C. Fritts, and R. H. Tolson (2006), Nonmigrating tides inferred from the Mars Odyssey and Mars Global Surveyor aerobraking data, *Geophys. Res. Lett.*, 33, L23201, doi:10.1029/2006GL027753.
- Wilson, R. J. (2002), Evidence for nonmigrating thermal tides in the Mars upper atmosphere from the Mars Global Surveyor Accelerometer Experiment, *Geophys. Res. Lett.*, 29(7), 1120, doi:10.1029/2001GL013975.
- Withers, P. (2006), Mars Global Surveyor and Mars Odyssey Accelerometer observations of the Martian upper atmosphere during aerobraking, *Geophys. Res. Lett.*, 33, L02201, doi:10.1029/2005GL024447.
- Withers, P., S. W. Bougher, and G. M. Keating (2003), The effects of topographically-controlled thermal tides in the martian upper atmosphere as seen by the MGS accelerometer, *Icarus*, 164, 14–32, doi:10.1016/S0019-1035.
- Wright, C. (2012), A one-year seasonal analysis of martian gravity waves using MCS data, *Icarus*, 219, 274–282, doi:10.1016/j.icarus.2012.03.004.
- Yiğit, E., and A. S. Medvedev (2009), Heating and cooling of the thermosphere by internal gravity waves, *Geophys. Res. Lett.*, 36, L14807, doi:10.1029/2009GL038507.
- Yiğit, E., and A. S. Medvedev (2015), Internal wave coupling processes in Earth's atmosphere, *Adv. Space Res.*, 55, 983–1003, doi:10.1016/j.asr.2014.11.020.
- Yiğit, E., A. D. Aylward, and A. S. Medvedev (2008), Parameterization of the effects of vertically propagating gravity waves for thermosphere general circulation models: Sensitivity study, *J. Geophys. Res.*, 113, D19106, doi:10.1029/2008JD010135.
- Yiğit, E., S. L. England, G. Liu, A. S. Medvedev, P. R. Mahaffy, T. Kuroda, and B. M. Jakosky (2015a), High-altitude gravity waves in the Martian thermosphere observed by MAVEN/NGIMS and modeled by a gravity wave scheme, *Geophys. Res. Lett.*, 42, 8993–9000, doi:10.1002/2015GL065307.
- Yiğit, E., A. S. Medvedev, and P. Hartogh (2015b), Gravity waves and high-altitude CO₂ ice cloud formation in the Martian atmosphere, *Geophys. Res. Lett.*, 42, 4294–4300, doi:10.1002/2015GL064275.